Nagano *et al.*
Progress in Earth and Planetary Science (2022) 9:57
https://doi.org/10.1186/s40645-022-00513-3

Progress in Earth and Planetary Science

RESEARCH ARTICLE Open Access

Spatiotemporal vertical velocity variation in the western tropical Pacific and its relation to decadal ocean variability

Akira Nagano[1*], Takuya Hasegawa[2,3] and Masahide Wakita[4]

Abstract: Prior to the cold phase of the Pacific decadal oscillation (PDO), sea surface water in the western tropical North Pacific is heated. To evaluate the impact of the subsurface water on the upper-ocean (< 100 m depth) temperature variation, we examined the vertical velocity variation. We applied altimetry-based gravest empirical mode (AGEM) method to Argo hydrographic profile (2001–2017) and altimetric sea surface height (1993–2017) data in the western tropical Pacific and obtained a time-varying three-dimensional (3D) potential density field in the layer from 100 to 1000 m depth. From the AGEM-derived potential density, we derived a 3D field of vertical velocity below 100 m depth by the P-vector inverse method, which is based on potential density and vorticity conservations, and examined the spatiotemporal characteristics, focusing on the seasonal to quasi-decadal (QD) variations. In the mean state, substantial upward current (> 10^{-6} m s^{-1}) is observed in the region of 10°–17°N, 140°E–180° in the North Equatorial Current, southern part of the North Pacific subtropical gyre. Possibly besides the Ekman upwelling, the upward current contributes to the cooling of the upper ocean in the western tropical North Pacific through the upward advection of the deep cold water. The upward current was found to be intensified (attenuated) by the strengthening (weakening) of the subtropical gyre interior southward flow on the QD timescale in association with frequent occurrences of La Niña (El Niño) events. The weakening of the upward current is responsible for the QD increase in upper-ocean temperature in the western tropical North Pacific, which is equivalent to or larger than 0.2 °C, several years after the warm phase of the PDO. The QD temperature variation may affect the phase reversal of the PDO through the heat transport of the western boundary current of the subtropical gyre, i.e., the Kuroshio.

Keywords: Western tropical Pacific, ENSO, PDO, Vertical velocity, P-vector inverse method, AGEM

1 Introduction

The subtropical gyre of the North Pacific is a basin-scale anticyclonic circulation, consisting of the northward swift western boundary current, so-called the Kuroshio, and the southward weak flow in the interior region. The subtropical gyre transports a huge amount of heat northward (e.g., Bryden and Imawaki 2001; Nagano et al. 2009, 2010). Through the variation in the northward heat transport, the subtropical gyre of the North Pacific is considered to play a critical role in interannual and longer timescale midlatitude climate variations such as the Pacific decadal oscillation (PDO) (e.g., Kawai et al. 2008), the most dominant variation in sea surface temperature (SST) in the North Pacific, (e.g., Mantua et al. 1997; Mantua and Hare 2002). Similar decadal oscillations were produced in ocean and atmosphere coupled numerical models (Latif and Barnett 1994, 1996; Gu and Philander 1997).

The spatial pattern of the PDO is defined as the first empirical orthogonal function (EOF) mode of SST in the North Pacific. A map of regression slope of SST to the PDO index (the time coefficient of the first EOF mode of

*Correspondence: nagano@jamstec.go.jp

[1] Center for Coupled Ocean-Atmosphere Research (CCOAR), Japan Agency for Marine-Earth Science and Technology (JAMSTEC), 2-15 Natsushima-cho, Yokosuka, Kanagawa 237-0061, Japan
Full list of author information is available at the end of the article

the SST) is illustrated in Fig. 1a. In the positive (warm) phase of the PDO, the pattern exhibits a negative SST anomaly in the central part of the North Pacific and a positive SST anomaly in the central and eastern equatorial Pacific (Mantua et al. 1997; Mantua and Hare 2002). Thermal disturbances excited at the northern periphery of the subtropical gyre due to the strengthening of the Aleutian Low are observed to subduct in the upper main thermocline (pycnocline), to propagate southward in the interior region of the subtropical gyre, and, longer than 10 years after the subduction, reaches a subsurface (up to approximately 100 m depth) layer around a latitude of 18°N of the western tropical North Pacific (e.g., Deser et al. 1996; Schneider et al. 1999).

By combined use of altimetric sea surface height (SSH) data, expendable bathythermograph temperature data, and Argo salinity data at lines from San Francisco to Hawaii and from Hawaii to Japan, Nagano et al. (2016a) studied the quasi-decadal (QD) variation in the subtropical gyre net heat transport due to the variation of the interior flow with periods of 8–12 years (e.g., Tourre et al. 2001; White et al. 2003; Hasegawa and Hanawa 2003; Hasegawa et al. 2013). Up to 4 years after the positive (warm) PDO phase, the volume transport-weighted temperature in the subtropical gyre interior region increases due to the enhancement in volume transport in a potential density layer between 25.0 and 25.5 σ_θ (σ_θ = potential density $-1000\ \mathrm{kg\,m^{-3}}$). As a result, because the temperature difference of the water masses transported by the Kuroshio and the gyre interior flow decreases, the northward net heat transport decreases. The reduction in the northward heat transport accumulates heat in the western tropical North Pacific, where climatological SST is very high, and enhances the warm pool SST (Nagano et al. 2016a), as is recognized in the map of the regression slope with a 3-year lag (Fig. 1d). In other words, the warm pool SST increases prior to the negative phase of the PDO.

The QD variation in the subsurface volume transport in the interior region of the subtropical gyre is suggested to contribute to the SST variation in the region of 10°–20°N, 125°–160°E in the western North Pacific warm pool (Nagano et al. 2016a) possibly through the enhancement of the upwelling of deep water from layers deeper than 100 m depth. If we obtain a three-dimensional (3D) field of vertical velocity, we can confirm this idea. The spatiotemporal characteristics of upward currents in the western tropical North Pacific are, however, unknown because vertical current velocity is too small ($< 10^{-4}\ \mathrm{m\,s^{-1}}$) to be directly measured by oceanographic instruments such as current meters, the accuracy of current measurements being of the order of $10^{-3}\ \mathrm{m\,s^{-1}}$ at best for now (e.g., Thomson and Emery 2014). Therefore, vertical velocity should be estimated from other physical variables such as 3D water density field under some hydrodynamic assumptions.

Based on the conservations of potential density and potential vorticity, Needler (1985) derived a formula of 3D absolute velocity vector ($\boldsymbol{v}$), in the interior region of subtropical gyres as

$$\rho \boldsymbol{v} = \frac{g\boldsymbol{k}\cdot(\nabla\rho\times\nabla q)}{\nabla(f\partial\rho/\partial q)\cdot(\nabla\rho\times\nabla q)}(\nabla\rho\times\nabla q), \tag{1}$$

where ρ is the potential density, f is the Coriolis parameter, g is the gravitational acceleration, $q = -f/\rho(\partial\rho/\partial z)$ is Ertel's potential vorticity neglecting the relative vorticity, and $\boldsymbol{k}$ is the unit vertical vector. In addition to potential density and potential vorticity, the Bernoulli function of a water parcel advected by the flow is conserved if the flow is steady and the diffusion can be neglected (e.g., Needler 1985; Pedlosky 1987a, b). For the estimation of the 3D current velocity field from hydrographic data, several methods have been proposed by past investigators (e.g., Stommel and Schott 1977; Olbers et al. 1985; Killworth 1983, 1986; Chu 1995, 2006). These methods are expected to provide similar 3D current velocity fields because they are based on the same assumptions, i.e., conservations of potential density and potential vorticity.

Chu (1995, 2006) developed a sophisticated method, called the P-vector inverse method, to calculate 3D absolute velocity vector from observed hydrographic data, avoiding cases that isosurfaces of potential density and potential vorticity are parallel (i.e., $\nabla\rho\times\nabla q = 0$), as described in the following section. For example, he applied the P-vector inverse method to the circulations in the upper layer of the North Atlantic and demonstrated a very strong downward velocity around a depth of the main pycnocline (500 m depth) in the area south of Iceland, where the subduction zone of the global ocean conveyor belt is possibly located (Schmitz 1995). Therefore, the P-vector inverse method provides reasonable 3D distributions of vertical velocity and may be used to diagnose vertical velocity in the western tropical and subtropical North Pacific.

By applying the P-vector inverse method to the 3D potential density field in the tropical and subtropical North Pacific, we expect to obtain a vertical velocity field in the upper ocean layer and to reveal its seasonal to decadal variations. In other words, we can identify the location where the QD variation in the subsurface volume transport in the interior region of the subtropical gyre reported by Nagano et al. (2016a) emerges in the western Pacific region and how the QD variation of the vertical transport to the east of the Philippines is related to the variation in the interior region. Further,

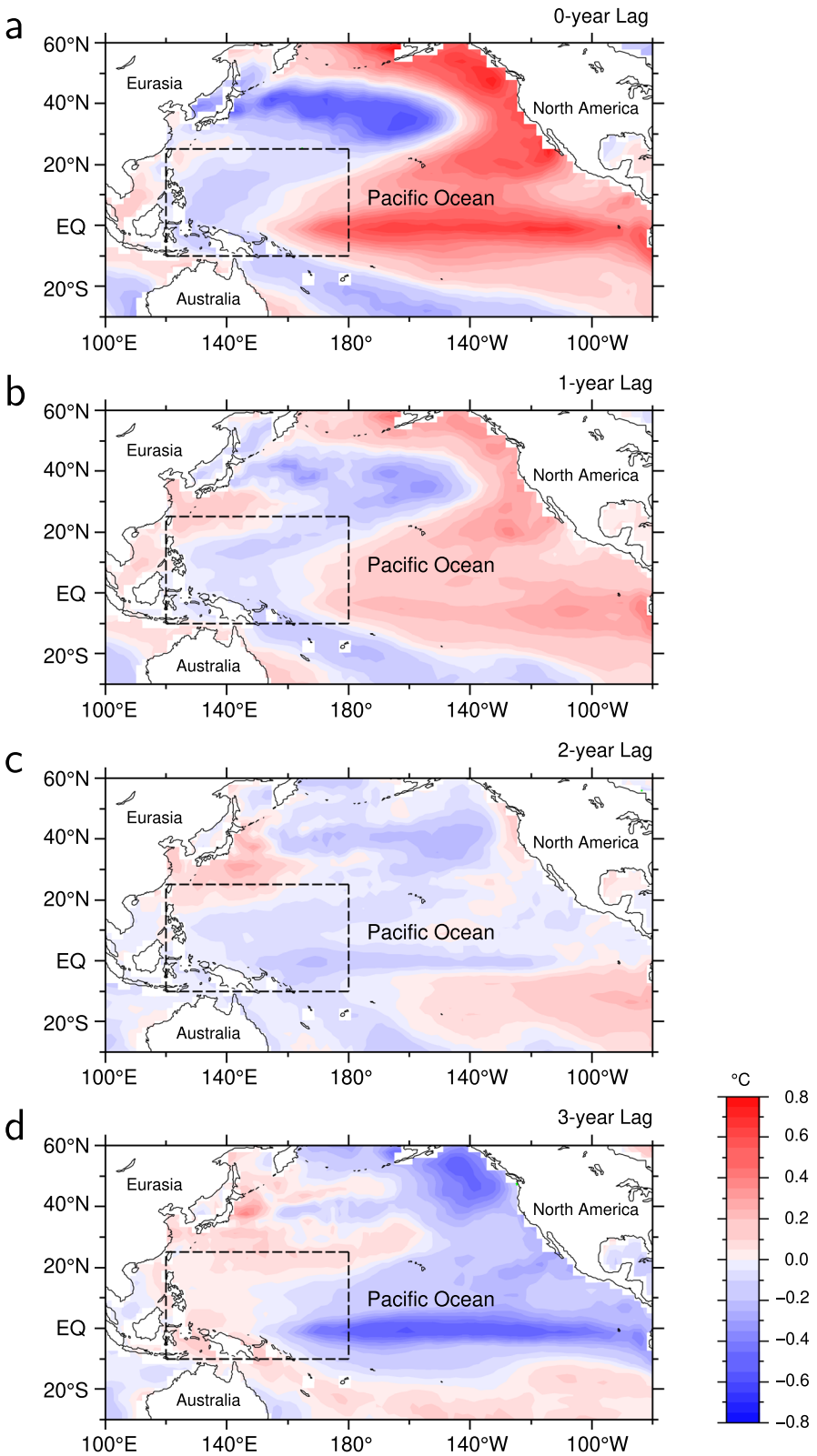

Fig. 1 Regression slope (°C) between the Pacific decadal oscillation (PDO) index and sea surface temperature (SST) anomaly with lags of **a** 0, **b** 1, **c** 2, and **d** 3 years. Dashed square shows the study region of this paper

the impact of the vertical transport on the upper ocean to the east of the Philippines may be estimated.

In general, potential vorticity is not conserved along streamlines with horizontal and vertical diffusion. To obtain the absolute velocity vector field by the P-vector method and other methods based on the potential vorticity conservation, a time-varying 3D gridded water density field with sufficient spatial resolution is required. As a candidate of such a dataset, we may use gridded hydrographic data such as the grid point value of the Monthly Objective Analysis using the Argo (MOAA GPV) data (Hosoda et al. 2008) based on global Argo float data collected since 2000. Using this dataset, we first attempted to compute the P-vector-derived vertical velocity. However, the vertical velocity computed from the MOAA GPV data applying the P-vector method is unreasonably large ($> 10^{-4}$ m s^{-1}) probably because the effective resolution (~1000 km) is too low to apply the conservation of potential vorticity. Hence, we must use a finer gridded dataset to obtain reliable vertical velocity estimates by the P-vector inverse method.

Satellite observations have extensive coverage and sufficient resolutions in space and time to resolve the ocean variations on scales ranging from mesoscale to global scale. SSH maps with a horizontal resolution of 1/4°×1/4° are available to examine current variations (Pujol and Mertz 2020). Particularly, because SSH is a physical parameter, which corresponds to integrated specific volume (i.e., reciprocal of water density) through the water column from the bottom to the sea surface, variations in altimetric SSH should be related to those in water density through the water column. Thus, combined use of the Argo hydrographic profile data and altimetric SSH data might produce a sufficiently fine resolution 3D hydrographic dataset.

The altimetry-based gravest empirical mode (AGEM) method has been applied to spatiotemporally sparse hydrographic data to estimate variations of hydrographic and current fields all over the world from SSH data (e.g., Sun and Watts 2001; Swart et al. 2010; Nagano et al. 2016a, b). Because AGEM-derived hydrographic fields have the same horizontal resolution as that of the altimetric SSH data, they are sufficient to resolve regional scale circulations and their temporal variations. Nagano et al. (2016a, b) applied the AGEM method to hydrographic data and altimetric SSH data, and estimated sections of potential temperature and salinity (therefore, potential density) at a line from San Francisco to near Japan via Hawaii across the interior region of the North Pacific subtropical gyre and 3D hydrographic fields in the western subarctic North Pacific.

In this study, we compute the 3D monthly potential temperature, salinity, and therefore potential density fields from the AGEM for areas divided by applying cluster analysis to Argo hydrographic profile data. We then estimate the vertical velocity field by the P-vector inverse method and examine the variations on seasonal to decadal timescales. In Sect. 2, we describe Argo conductivity–temperature–depth (CTD) profile data, altimetric SSH data, and the AGEM method. In Sects. 3 and 4, we analyze the AGEM-derived potential density and the P-vector-based vertical velocity fields, focusing on their variations related to the QD variations in the tropical and subtropical North Pacific and examine the impact of the vertical velocity variation on the upper-ocean temperature through the vertical advection of the deep cold water. Summary and conclusion are provided in Sect. 5.

2 Data and methods

2.1 Argo data

To construct AGEM fields, we used more than 7000 temperature and salinity profiles from the near sea surface (10 dbar) to a pressure level of 1000 dbar (equivalent to a depth of approximately 1000 m) collected for each month by Argo floats (Advanced automatic QC Argo Data version 1.2) from January 2001 to May 2017 in the region of 10°S–25°N, 120°E–180°. A total of 90192 hydrographic profiles were used in this study. The accuracies of the Argo temperature, salinity, and pressure data were reported to be ±0.005 °C, ±0.01 (psu), and ±5 dbar by Argo Science Team, respectively (Hosoda et al. 2008). Following the Akima (1970) method, temperature and salinity profiles were interpolated onto the vertical grids at intervals of 10 dbar from 10 to 1000 dbar.

From the Argo temperature and salinity profile data, we calculated spiciness parameter by using the polynomial proposed by Flament (2002), which isopleths are orthogonal to those of potential density on the temperature–salinity diagram. The orthogonal character of the spiciness parameter permits us to identify water masses in terms of potential density by the single parameter. Because of this, spiciness analyses are useful to distinguish water masses, as demonstrated in the Kuroshio and North Pacific subtropical gyre interior regions by Nagano et al. (2009, 2010, 2012). We performed cluster analysis, applying Ward's criteria (e.g., Ward 1963; Anderberg 1973) to spiciness values averaged between isopycnal layers at intervals of 0.01 kg m^{-3} from 24.06 to 26.46 σ_θ and changing the number of clusters from 3 to 9. The number of clusters being set to 7, the classification based on the cluster analysis is found to be roughly consistent with the distributions of water masses in the western tropical and subtropical Pacific such as the North/South Pacific Tropical Waters and the North Pacific/Antarctic Intermediate Waters (e.g., Fine et al. 1994; Kashino et al. 2011; Talley et al. 2011). Thus, we classified Argo hydrographic profiles into 7 clusters.

We divided the study region (10°S–25°N, 120°E–180°) into pieces of 5° on each side based on this cluster analysis result. Next, the dominant (the most frequent) cluster of hydrographic profiles for each piece was determined. Based on the dominant clusters in all pieces, the study region was separated into 7 areas in individual months except for January (6 areas) and February (5 areas). The area division based on the cluster analysis is found to be roughly consistent with the regional current and water mass pathways (Fig. 2) (e.g., Reid 1997; Talley et al. 2011).

Using the Argo temperature and salinity profiles, we calculated the dynamic height with the reference pressure level of 1000 dbar, H_{CTD}, in meters as

$$H_{\mathrm{CTD}} = \frac{1}{g}\int_{10\,\mathrm{dbar}}^{1000\,\mathrm{dbar}} \delta\,\mathrm{d}p, \tag{2}$$

where p is pressure and $\delta = \rho^{-1} - \rho^{-1}(0, 35, p)$ is the specific volume anomaly relative to the specific volume of seawater with temperature 0 °C and salinity 35 (e.g., Gill 1982) calculated from Argo CTD data. The vertical

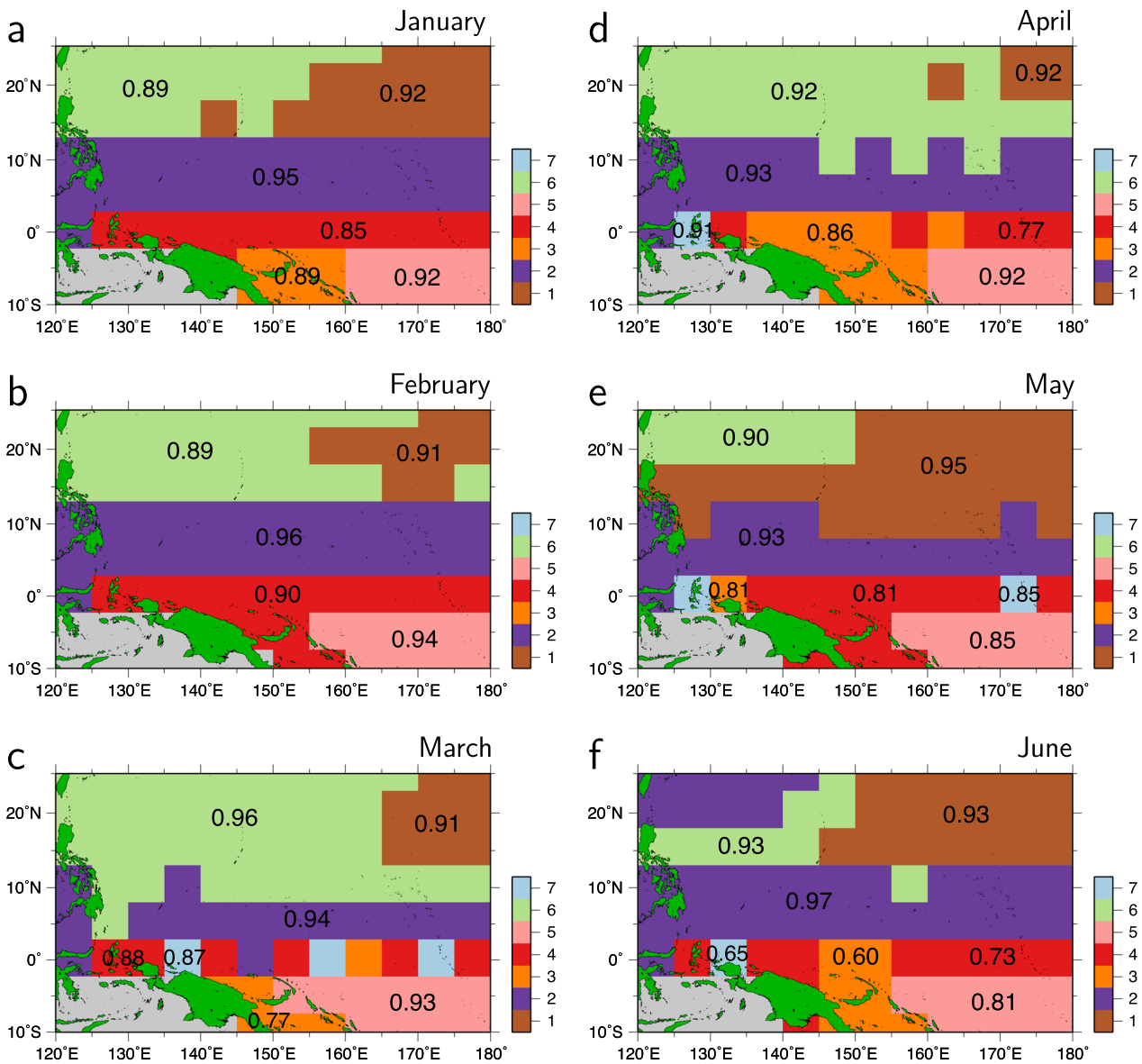

Fig. 2 Divisions of the study region up to 7 areas applying the cluster analysis to Argo CTD profiles collected from **a** January to **l** December. Area numbers from 1 to 7 are indicated in the color bar in the lower right corner of each panel. Numeric values in areas divided by the cluster analysis indicate correlation coefficients between altimetric SSH and sea surface dynamic height relative to the pressure level of 1000 dbar

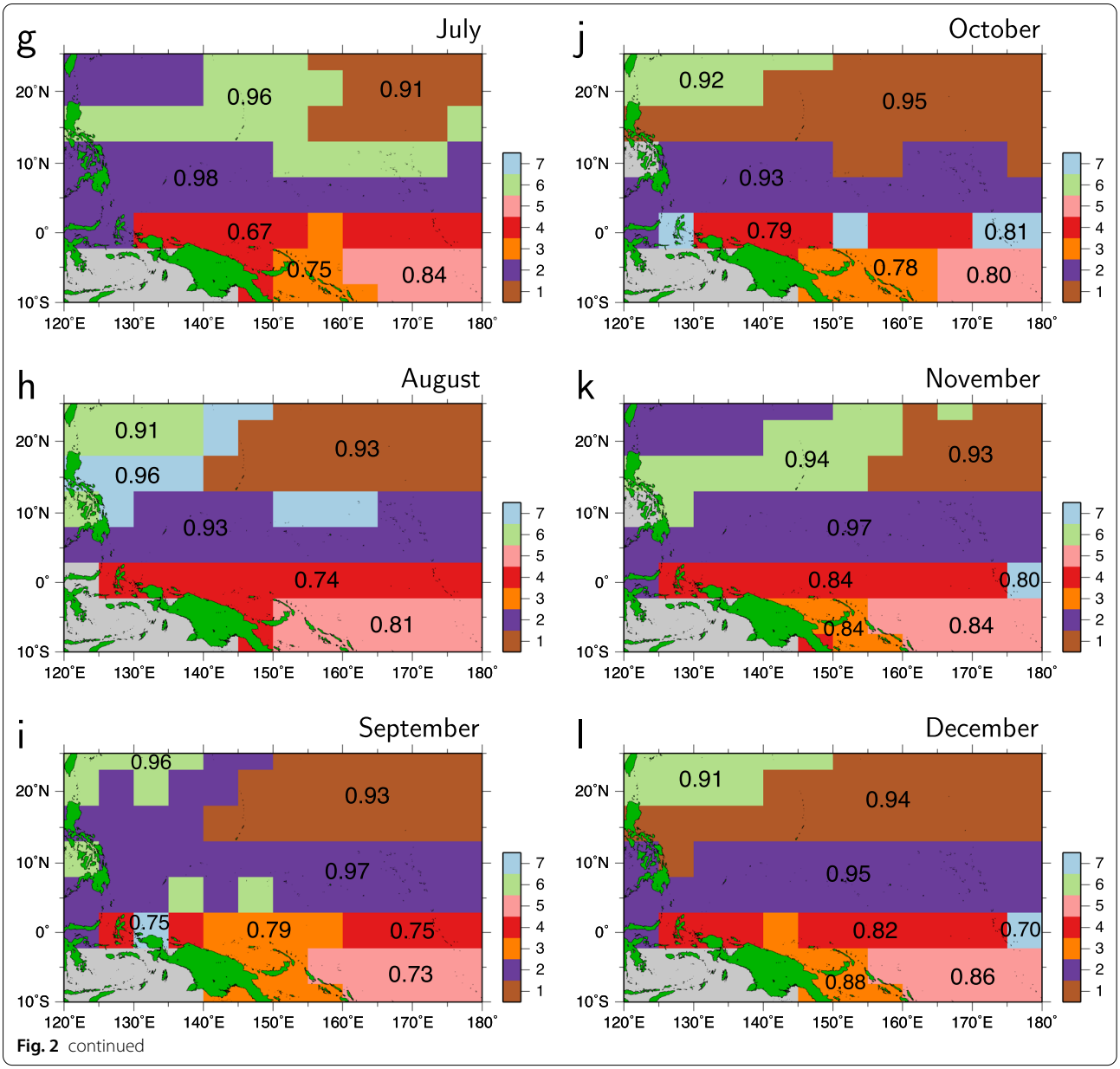

Fig. 2 continued

integral in Eq. (2) was discretized into the summation of 10-dbar averaged δ multiplied by the vertical interval of 10 dbar from 10 to 1000 dbar. The error in the Argo-derived H_{CTD} was estimated to be smaller than 0.8 cm, which is small compared with the altimetric SSH data error (~3 cm).

2.2 Altimetric SSH data

We used daily altimetric absolute SSH (H_{ALT}) 1/4° × 1/4° gridded map data in the region of 10°S–25°N, 120°E–180° from January 1993 to May 2017. The absolute SSH data are derived from the delayed-time updated SSH (Level 4) anomaly data (DT_SLA-H) (Pujol and Mertz 2020) added to the mean dynamic topography data (MDT_CNES-CLS13) provided by Rio et al. (2011). Because the SSH data are erroneous near the coasts, we did not use SSH data in regions of water depths less than 1000 m to estimate AGEM fields and AGEM-derived 3D potential temperature and salinity fields.

H_{ALT} is linearly correlated with the dynamic height derived from Argo CTD data, i.e., H_{CTD}, with correlation coefficients of 0.60–0.98 (Fig. 2), which are much higher than the 1% significance level (i.e., within the 99%

confidence limit) based on the Student's t test. Therefore, we performed linear regressions and based on those equations, converted values of H_{ALT} to dynamic height, which is required to construct 3D potential temperature and salinity fields by the AGEM method described in the next subsection. Note that the correlation coefficients in the equatorial and South Pacific are relatively low possibly because of high-frequency (time scales shorter than days) variations by internal gravity waves or small scale patchy water masses as observed by Richards et al. (2015) and others, which cannot be fully resolved by the altimetric SSH observations.

2.3 Area-wise AGEM method

Vertical structures of temperature and salinity are considered to be greatly different among the areas classified by the cluster analysis and seasons. Thus, to consider the spatial and seasonal variations, for each month and each area, we constructed AGEM fields, i.e., the relations between hydrographic profiles and dynamic height, H_{CTD}, based on all the Argo CTD data in the area during the month. The AGEM fields were smoothed for H_{CTD} by a Gaussian weight function with an e-folding scale of 2.5 cm to remove noisy features due to the high-frequency variability.

As an example, the AGEM potential temperature and salinity fields down to a depth of 1000 m for 6 areas in January are shown in Figs. 3a–f and 3g–l, respectively. The main thermocline illustrated by the sharp potential temperature decrease from 25 °C to 8 °C commonly deepens as the dynamic height H_{CTD} increases. Along with the main thermocline, the salinity maximum layer deepens with H_{CTD} although the salinity values are different for each area. Salinity in the areas in the Southern Hemisphere (Fig. 3i, k) is higher than that in other areas (Fig. 3g, h, j, l), as illustrated by Reid (1997) and others. Corresponding to the regional differences in salinity, there are also regional variations in potential temperature and density.

We identify differences in the vertical distributions of potential temperature and salinity for the season (not shown). In the upper layer shallower than 100 m, potential temperature, and salinity seasonally vary associated with the development of the mixed layer in winter and the stratification in summer. Because, in this AGEM estimation, we used Argo hydrographic data during approximately 17 years from 2001 to 2017, the constructed AGEM fields should account the interannual to decadal variations. Such spatial and seasonal variations of the AGEM fields beside the SSH variations are responsible for those of the horizontal circulation and vertical current and their interannual to decadal modulations, as described in the following sections.

By converting monthly altimetric SSH, H_{ALT}, to H_{CTD} and referring to the AGEM fields, we estimated the temporal changes of the 3D fields of potential temperature and salinity, and that of potential density on the horizontal grids of 1/4° at the vertical grids of 10 m from 10 to 1000 m. Ranges of converted SSH, i.e., dynamic height, variations in individual areas were within those of the dynamic height of the AGEM fields (abscissa in Fig. 3). This suggests that the AGEM-derived 3D potential temperature and salinity fields involve the seasonal to decadal variations that are consistent with the SSH variations. To eliminate noisy features and to suppress artificial gaps between the areas in AGEM-derived potential temperature and salinity fields for reasonable estimation by the P-vector inverse method, spatial smoothing was performed using a Gaussian filter with a damping scale of 150 km. For the following analysis, we used the smoothed AGEM-derived potential temperature and salinity fields. In Fig. 4, we show the root-mean-square (RMS) potential density differences between Argo and AGEM-derived data at depths of 100, 200, 400, and 800 m; the RMS potential density difference at each grid was computed by using data collected in the month by Argo floats within a radius of 1000 km. The RMS potential density differences are reduced with the depth from approximately 1.2 $\mathrm{kg\,m^{-3}}$ at 100 m to 0.1 $\mathrm{kg\,m^{-3}}$ at 800 m due to the weakening of the variations on shorter timescales than approximately 1 month. In addition, note that there are no artificial spatial gaps in the RMS potential density differences due to the area division based on the cluster analysis.

Figure 5a shows the horizontal distribution of potential density at a depth of 200 m averaged in all months during the study period. In addition, according to Rintoul et al. (2002) and Nagano et al. (2016b), we calculated the streamfunction defined as

$$\chi_{1000} = \frac{1}{g}\int_{10\,\mathrm{dbar}}^{1000\,\mathrm{dbar}} p\,\delta\,\mathrm{d}p. \tag{3}$$

The streamfunction in the mean state integrated from the sea surface to a pressure level of 1000 dbar (approximately 1000 m depth) is illustrated by contours in Fig. 5a. The estimated mean current circulations are similar to those observed by past investigators (e.g., Nitani 1972; Reid 1997; Qu et al. 1998; Qu and Lukas 2003). The North Pacific subtropical and tropical gyres to the north and south of approximately 13°N are characterized by high and low potential density. Associated with the northward sharp decrease in potential density at a latitudinal band between 10°N and 15°N, there exists a strong current toward the western boundary of the Pacific basin, i.e., the North Equatorial Current (NEC), which consists of the

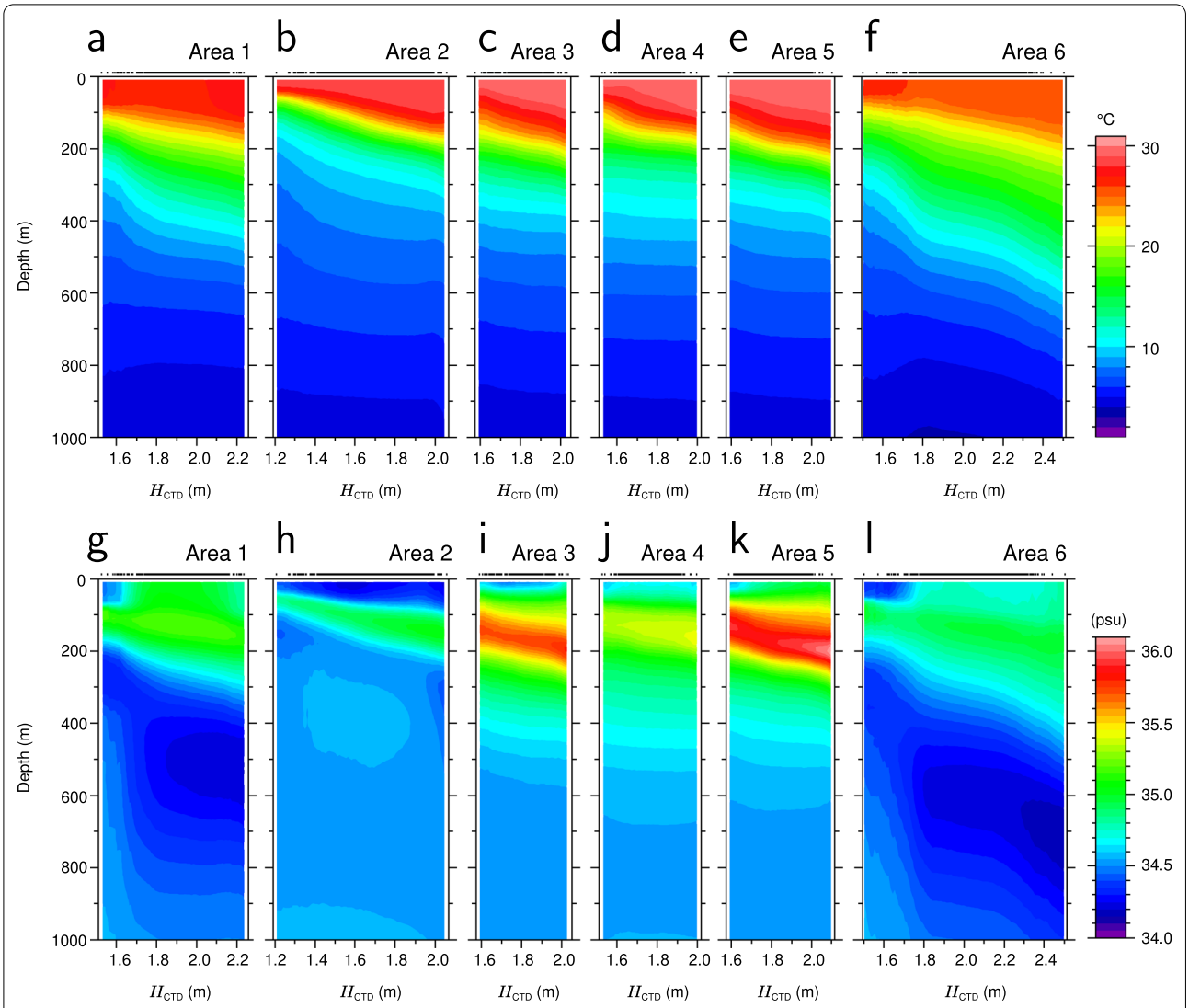

Fig. 3 AGEM (**a**–**f**) potential temperature (°C) and (**g**–**h**) salinity fields for January in terms of dynamic height relative to a pressure level of 1000 dbar, H_{CTD}, (m). AGEM potential temperature (salinity) fields from area 1 to area 6 are displayed in panels from **a** (**g**) to **f** (**l**). Ordinate is depth (m) and abscissa is H_{CTD}. Dots at the top of each panel denote values of the dynamic height based on Argo-observed CTD data

westward current of the southern part of the subtropical gyre and that of the northern part of the tropical gyre.

The Mindanao Dome (MD) is produced in the region off the eastern coast of the Mindanao Island (4°–10°N) and the eastern edge of the circulation extends to the east of 140°E in boreal spring (Fig. 5c) and to the east of 150°E in boreal autumn (Fig. 5e). The remarkable seasonal change of the circulation observed by Qu et al. (1998), Qu and Lukas (2003), and others, and produced in a numerical model by Tozuka et al. (2002) are reproduced in this AGEM estimation.

2.4 P-vector inverse method

By using a unit vector $\boldsymbol{P}$, called the perfect vector (P-vector); and the magnitude of the velocity vector γ, called the speed parameter, at location $\boldsymbol{x} = (x, y, z)$, Chu (1995, 2006) expressed Eq. (1) as $\boldsymbol{v}(\boldsymbol{x}) = \gamma \boldsymbol{P}$. Here, using potential density ρ and potential vorticity $q = -f/\rho(\partial\rho/\partial z)$, $\boldsymbol{P}$ is defined as

$$\boldsymbol{P} = (P_x, P_y, P_z) = (\nabla\rho \times \nabla q)/|\nabla\rho \times \nabla q|. \tag{4}$$

Using the thermal wind equation, γ at a depth level of z_k (γ_k) is calculated as

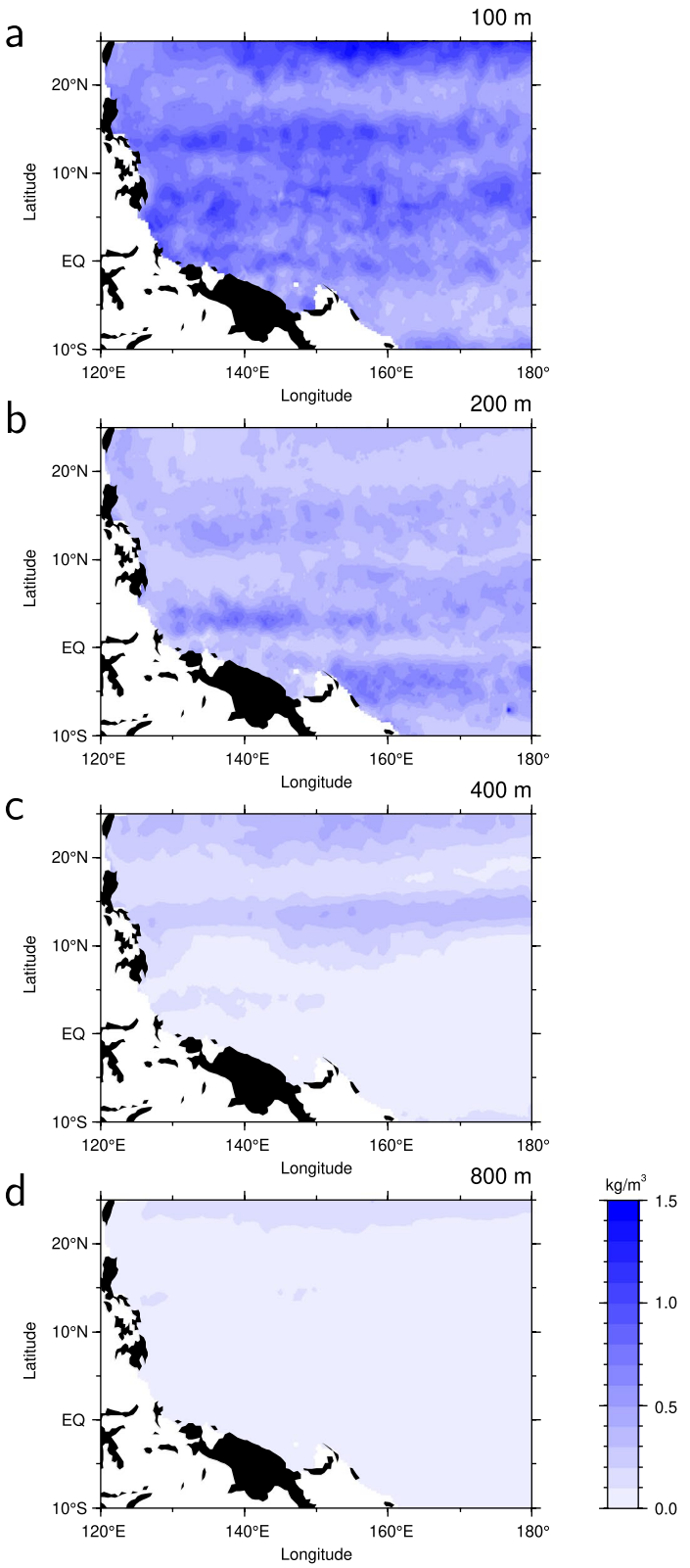

Fig. 4 Root-mean-square difference between AGEM-derived and Argo-observed potential density at depths of **a** 100, **b** 200, **c** 400, and **d** 800 m

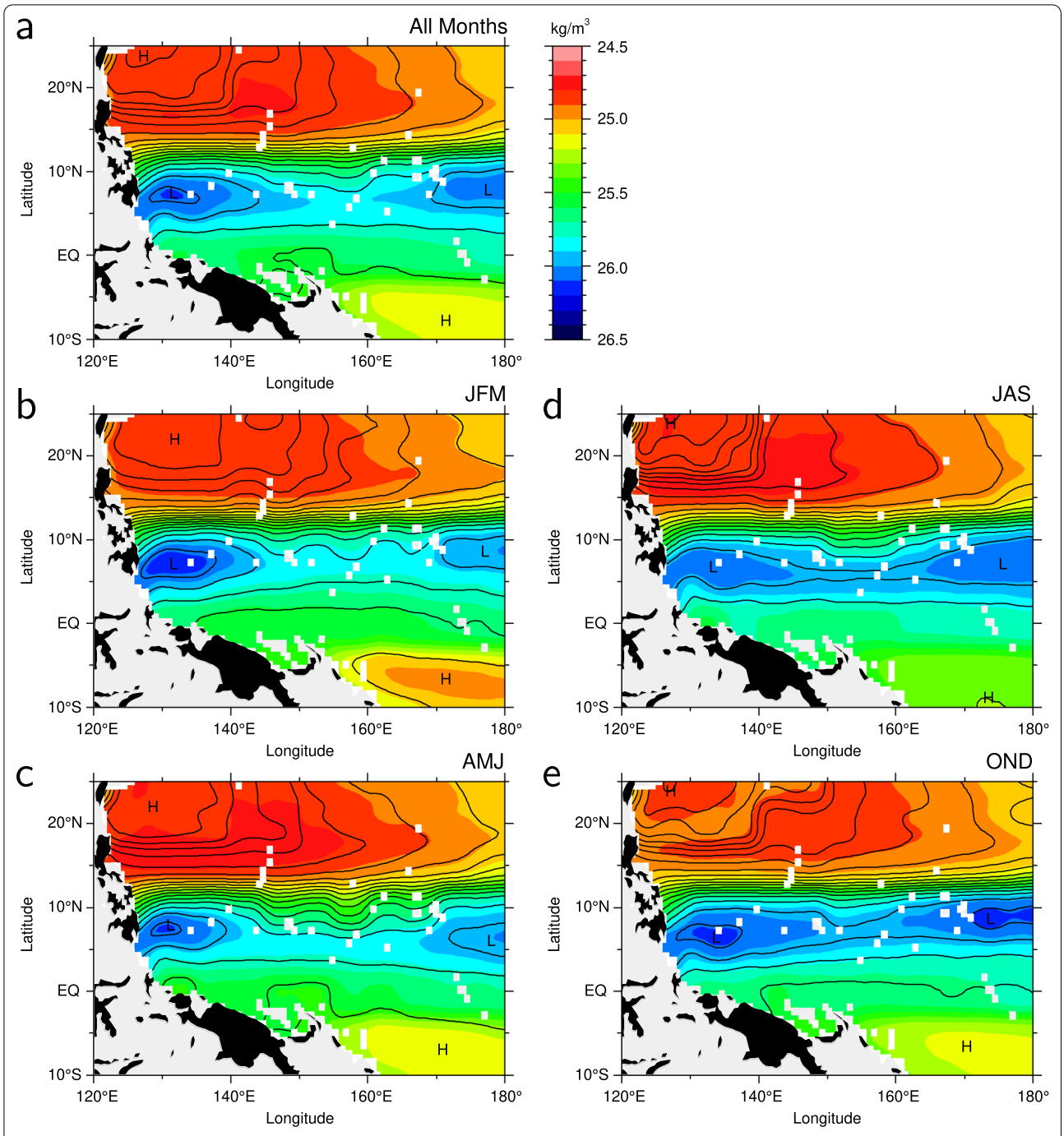

Fig. 5 Horizontal distributions of AGEM-derived potential density σ_θ at a depth of 200 m (kg m^{-3}, color shading) and streamfunction χ_{1000} (M kg s^{-1}, contours) averaged in **a** all months, **b** January–March, **c** April–June, **d** July–September, and **e** October–December during 1993–2016. Contour intervals of streamfunction are 0.1 M kg s^{-1}. Letters H and L indicate maxima and minima of streamfunction, respectively

$$\gamma_k = \begin{vmatrix} \Delta u_k & P_x^{(r)} \\ \Delta v_k & P_y^{(r)} \end{vmatrix} \Big/ \begin{vmatrix} P_x^{(k)} & P_x^{(r)} \\ P_y^{(k)} & P_y^{(r)} \end{vmatrix}, \tag{5}$$

where $(\Delta u_k, \Delta v_k)$ is the vertical shear vector of horizontal velocity relative to the reference depth level, z_r. In this study, we set z_r to 1000 m.

Using the monthly 3D potential density fields estimated by the area-wise AGEM method, we calculated

the 3D velocity vector below a depth of 100 m, where the AGEM-based potential density is reliable. Note that we did not conduct the calculation in the equatorial region between 3°S and 3°N because $|f|$ is close to zero approaching the equator. There are two necessary conditions for the solution to exist. Isosurfaces of potential density and those of potential vorticity are not parallel ($\nabla\rho \times \nabla q \neq 0$), and the denominator of Eq. (5) does not vanish (for the existence of the P-spiral). By examining the two necessary conditions for the existence of the absolute velocity vector, we can remove inappropriate solutions. In this study, we did not calculate the P-vector and the speed parameter in the locations where these necessary conditions are not satisfied. The necessary conditions are satisfied in areas exceeding 86% of the calculation region every month. Values of $\boldsymbol{P}$ and γ in areas with no data were interpolated with a spatial Gaussian weight function with a horizontal e-folding scale of 150 km, which is much smaller than spatial scales of the phenomena of our interests (> 500 km).

The estimation of the 3D absolute current velocity field was conducted under some assumptions. In particular, the neglect of relative vorticity may produce significant error in the vertical velocity. Taking the curl of the momentum equation and using the continuity equation for incompressible fluid, we obtain $\partial w/\partial z = (1/f)(\partial\zeta/\partial t)$, where $\zeta = \partial v/\partial x - \partial u/\partial y$ is relative vorticity (e.g., Gill 1982). The horizontal velocity is no more than 50 cm s^{-1} in the NEC and the horizontal scale of the variation is larger than 1000 km, so that the magnitude of ζ is order of 10^{-7} s^{-1} except in the western boundary region. Taking into account the vertical and time scales of the w variation, 100 m and 1 month, respectively, the contribution of relative vorticity except in the western boundary region is less than 10^{-6} m s^{-1}, which is smaller than the w variation. In the western boundary region, the error larger than 10^{-6} m s^{-1} is considered to be included in the estimated vertical velocity data.

By using the thermal wind equation, the vortex-stretching equation, $v = (f/\beta)\partial w/\partial z$, gives $\rho\partial^2 w/\partial z^2 = -(\beta g/f^2)\partial\rho/\partial x$, where β is the latitudinal variation of f (Killworth 1983). On the basis of this equation, the error of the estimated vertical velocity attributed to the potential density error can be evaluated. The RMS difference between Argo and AGEM-derived potential density data in layers deeper than the main thermocline, where variations possibly due to high-frequency internal gravity waves are relatively small, may be regarded as the AGEM potential density error. If we set the error of the potential density to 0.1 kg m^{-3}, we evaluate the error of the w variation with a horizontal scale of 1000 km and a vertical scale of 100 m to be 10^{-7} m s^{-1}. The error is one order of magnitude smaller than the variation in w on the seasonal and longer time scales, as will be discussed in the following sections.

To examine the characteristics of interannual and longer timescale variations in vertical velocity, we smoothed the data by a 15-month running mean filter. We decomposed the interannual vertical velocity variation by EOF modes to reveal regional-scale variation patterns, as the EOF mode decomposition is helpful to examine the spatiotemporal characteristics of the variations (e.g., Thomson and Emery 2014). Based on the EOF mode patterns, we determine the upwelling region where we compute volume and temperature transports.

2.5 SST data

To examine the impact of vertical velocity on upper-ocean (< 100 m depth) temperature in the region east of the Philippines, we used monthly US National Oceanic and Atmospheric Administration (NOAA) Optimum Interpolation Sea Surface Temperature (SST) V2 (NOAA_OI_SST_V2) data (Reynolds et al. 2002) from January 1993 to May 2017 in the region of 10°S–25°N, 120°E–180°. We smoothed the data by a 15-month running mean filter to eliminate the seasonal variation and evaluated the temporal tendency of the temperature by taking the smoothed data to the water temperature averaged in the top 100 m.

2.6 Climate indices

We used the Niño 3.4 index from January 1993 to December 2016, which is defined as the monthly mean SST anomaly from the seasonal variation in the central and eastern equatorial region of 5°N–5°S, 170°W–120°W as an El Niño–Southern Oscillation (ENSO) index by Trenberth (1997). Anomalously high and low SST events in the central and eastern equatorial Pacific, i.e., El Niño and La Niña events, are indicated by the Niño 3.4 index. In addition, the PDO index from January 1993 to December 2016, defined as the time coefficient of the first EOF mode of SST in the region poleward of 20°N for the period from 1900 to 1993 (Mantua et al. 1997), was used to calculate the regression slope between the PDO index and SST in the Pacific (Fig. 1) and to conduct comparison with the time series of the vertical current transports in the western tropical North Pacific.

3 Results

3.1 Mean circulation and vertical velocity fields

The area-wise AGEM estimation produced the horizontal upper-ocean circulations in the western parts of the North Pacific subtropical gyre and the North/South

Pacific tropical gyres, as illustrated by the streamfunction in Fig. 5a. Feeding the subtropical gyre interior southward flow, the westward flowing NEC is strengthened toward the western boundary from 148°E to 135°E (Fig. 5a). The cyclonic circulation of the MD centered around 8°N, 130°E is separated from the eastern tropical cyclonic circulation east of 165°E. Associated with the westward shrinkage of the MD in boreal winter (Fig. 5b) and spring (Fig. 5c), the westward current of the southern part of the NEC around a latitude of 8°N is attenuated in longitudes between 145°E and 168°E as illustrated by the widening and undulation of the χ_{1000} contours. When the MD is weak, the NEC approaches the North Equatorial Countercurrent (NECC), and it generates wavy patterns between the currents. The wavy patterns may be attributed to fluctuations due to the barotropic instability (e.g., Pedlosky 1987a), which can occur in the enhanced horizontal shear between the opposing currents, as observed in the central and eastern equatorial regions (e.g., Tanaka and Hibiya 2019). In boreal summer (Fig. 5d) and autumn (Fig. 5e), the MD extends eastward and strengthens the NEC.

Upward (positive) velocities of approximately 1×10^{-6} m s^{-1} are found in a part of the NEC, 10–16°N, 140°E–180°, in layers of 100 m (Fig. 6a) and 200 m (Fig. 6b) depths. This upwelling region is located in the boundary between the subtropical and tropical gyres, where the meridional gradients of the potential density and streamfunction are remarkable (Fig. 5a). Meanwhile, at a depth of 400 m, there is no systematic pattern of vertical velocity. As indicated by the vertical velocity maps at 100 m depth in Fig. 7, the upward velocity is extensively observed in the region north of approximately 10°N, mostly in the subtropical gyre region, in boreal winter (Fig. 7a) and spring (Fig. 7b) but is limited in the latitudes south of 15°N in summer (Fig. 7c) and autumn (Fig. 7d). The magnitudes of the vertical velocity tend to be amplified in low latitudes near the western boundary regions because of $\gamma\sim f^{-1}$ as derived from Eq. (5). Although values of vertical velocity at individual grids are similar to or a little larger than the error (10^{-6} m s^{-1}) estimated in Sect. 2.4, the error of mean value across such a regional scale (> 2000 km) is evaluated to be 10^{-8} m s^{-1}. Therefore, we focus on the variations with spatial scales equivalent to or larger than the upwelling region in the NEC. In Sect. 3.3, we will discuss the vertical volume and temperature transports across the upwelling region.

The seasonal changes in vertical velocity are also identifiable in the zonal and meridional sections; for example, we show zonal sections at the latitude of 12.6°N (Fig. 8) and meridional sections at the longitude of 145.4°E (Fig. 9). The upward and downward velocities were produced in a layer down to a depth of approximately 350 m in association with the undulation of the isopycnal surfaces of 25.0–26.5 σ_θ in the longitudinal band between 140°E and 170°E. The intensity of the vertical velocity is greatest in boreal winter (Figs. 8b, 9b) and spring (Figs. 8c, 9c). In the region from 140°E to 160°E, the upward velocity appears to be stronger than the downward velocity; particularly, in the layer shallower than 150 m, upward velocity is predominant (Fig. 8).

The considerably large vertical velocity (> 5×10^{-6} m s^{-1}) is generated in winter and spring around a latitude of 12°N, where the main pycnocline sharply shoals toward the equator along with the strongly baroclinic NEC, as illustrated in Fig. 9b, c. The strong vertical velocity in boreal winter to spring is considered to be driven by the winter intensification of the NEC, which may be partly attributed to the variation of the subtropical gyre interior flow volume transport in a potential density layer of 25.0–25.5 σ_θ reported by Nagano et al. (2012, 2016a). Despite the great seasonal change in a layer between 150 and 350 m depths, the seasonal change in the shallower layer around a latitude of 10°N between 140°E and 180° is remarkably small. Beneath a depth of approximately 350 m, where the vertical potential density gradients are less than those in the overlying layer, the magnitudes of the vertical velocity are unsubstantial.

3.2 Interannual and longer timescale variations in vertical velocity

The vertical velocity field varies on various time scales longer than 1 year. As described in Sect. 2.4, we obtained the interannual variation in vertical velocity by a 15-month running mean filter and calculated the EOF modes. The percentages of variance explained by the first and second EOF modes are 66% and 11%, respectively, and the sum of these modes explains 77% of the total variance. Each higher EOF mode accounts for no more than 3% of the total variance. Therefore, the leading two EOF

(See figure on next page.)

Fig. 6 Horizontal distribution of vertical velocity *w* at depths of **a** 100, **b** 200, and **c** 300 m. Vertical velocity was estimated by the P-vector inverse method from the AGEM-derived potential density field. Positive values show upward velocity. Contour intervals are 1×10^{-6} m s^{-1}. Gray shadings indicate regions of no data because of small values of the Coriolis parameter and shallow water depth. Zonal and meridional thin solid lines denote locations of the *w* sections shown in Figs. 8a and 9a. Dotted square delineates the region where Nagano et al. (2016a) studied the QD variation in SST. In the solid square, vertical volume and temperature transports and SST tendency due to the vertical current variation were calculated as in Fig. 14

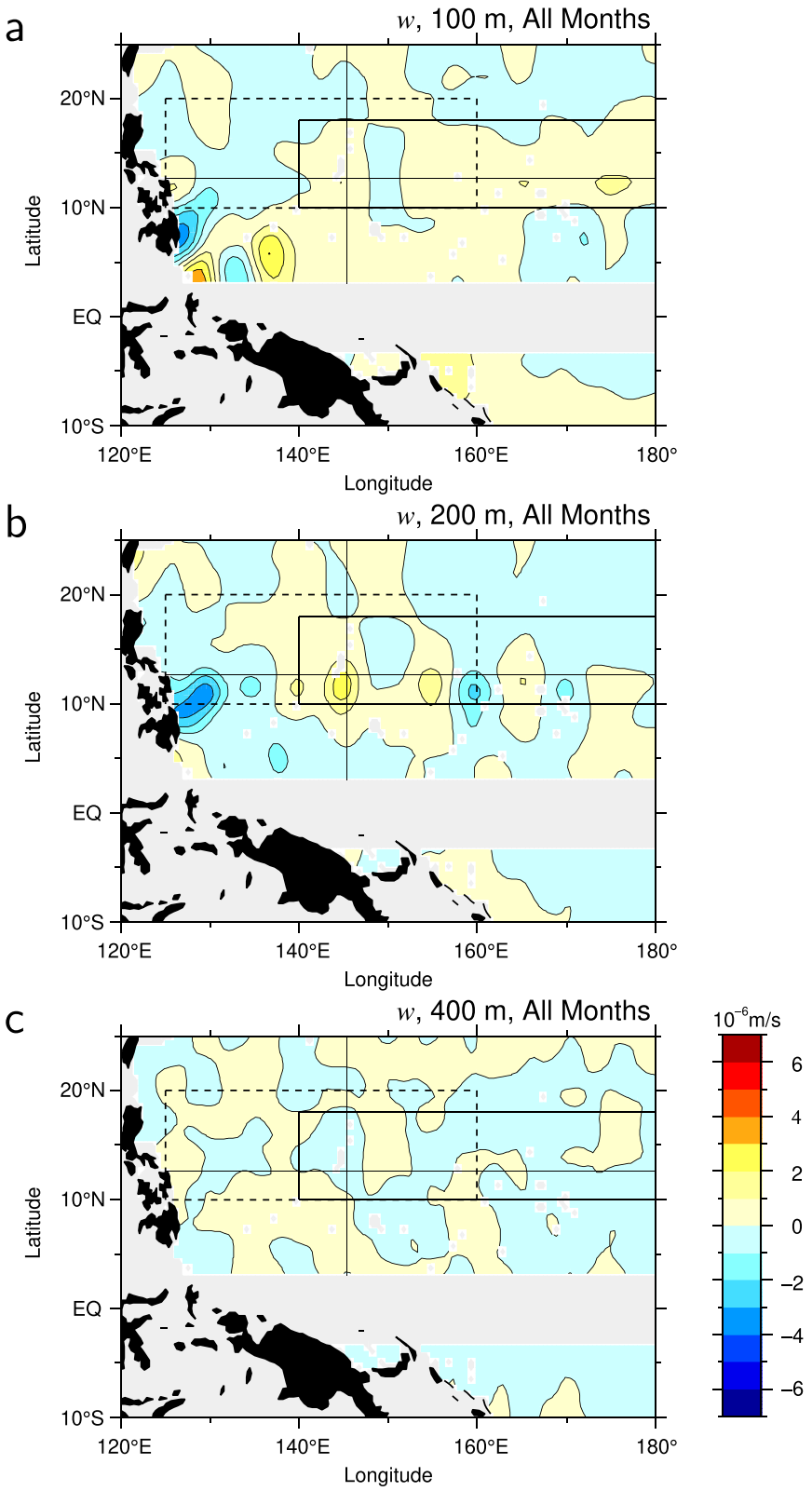

Fig. 6 (See legend on previous page.)

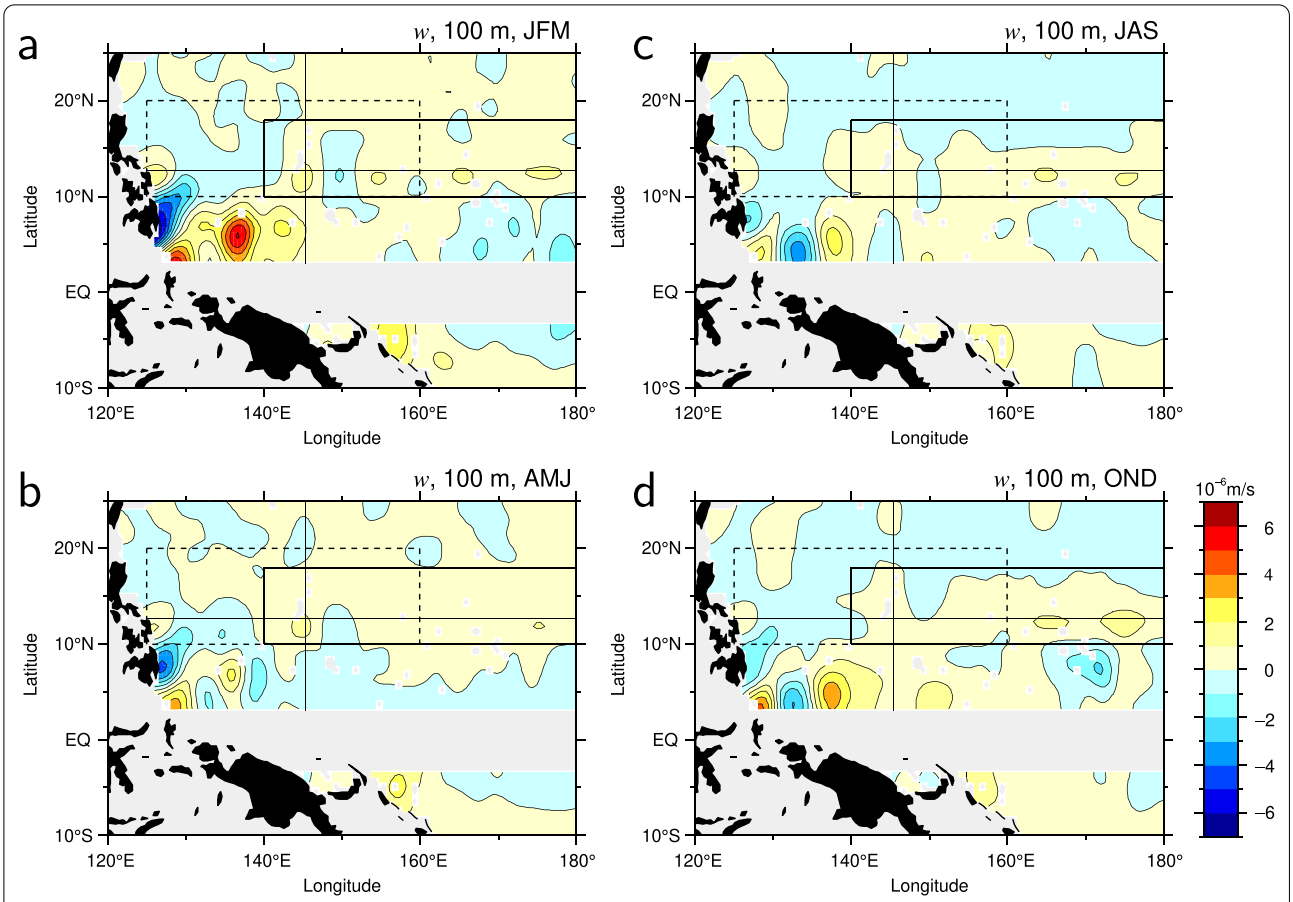

Fig. 7 Horizontal distribution of vertical velocity w at a depth of 100 m averaged in **a** January–March, **b** April–June, **c** July–September, and **d** October–December during 1993–2016. Positive values show upward velocity. Contour intervals are 1×10^{-6} m s^{-1}. Gray shadings indicate regions of no data because of small values of the Coriolis parameter and shallow water depth. Zonal and meridional thin solid lines denote locations of the w sections shown in Figs. 8b–e and 9b–e. Dotted square delineates the region where Nagano et al. (2016a) studied the QD variation in SST. In the solid square, vertical volume and temperature transports and SST tendency due to the vertical current variation were calculated as in Fig. 14

modes can explain most of the interannual to decadal vertical velocity variations.

The horizontal patterns of the first EOF mode at depths of 100 and 200 m are shown in Fig. 10a, b, respectively. At 100 m depth, apart from the western boundary region, the first EOF mode varies with a zonal scale exceeding 2000 km such as in the negative loading region of 10°–15°N, 150°E–180° (Fig. 10a), where the mean vertical velocity is largely upward, containing smaller scale (∼1000 km) variations (Fig. 6a). The positive and negative alternating large loadings are present to the east of Mindanao Island (3°–10°N, 125° –140°E), but, because relative vorticity was not taken into account, the vertical velocity estimated in the western boundary current region may be unreliable.

At a depth of 200 m (Fig. 10b), remarkably large positive and negative loadings are aligned alternatively along a latitude of 12°N with a zonal scale of approximately 500 km. The zonal scale of the vertical velocity variation at this depth is smaller than that at 100 m depth. The area of either sign of the loading at 200 m depth appears not to be dominant in the region 10°–15°N, 150°E–180°. In both zonal (Fig. 10c) and meridional (Fig. 10d) sections of the EOF mode, the remarkable variation is observed down to a depth of approximately 350 m, below which vertical gradient of potential density is small and the vertical velocity variation is weak. Therefore, the first EOF mode variation of the vertical velocity is responsible for the intensity change of the upward current above approximately 350 m depth in the region of 10°–17°N, 140°E–180° shown in Figs. 6, 8a, and 9a.

The second EOF mode of the vertical velocity at a depth of 100 m has a large negative loading in a region similar to the first EOF mode but is limited within the region of 10°–15°N, 155°E–180° (Fig. 11a). Regions equatorward of 10°N and 10°S show mostly positive values. At a depth of 200 m (Fig. 11b), positive and negative loadings with

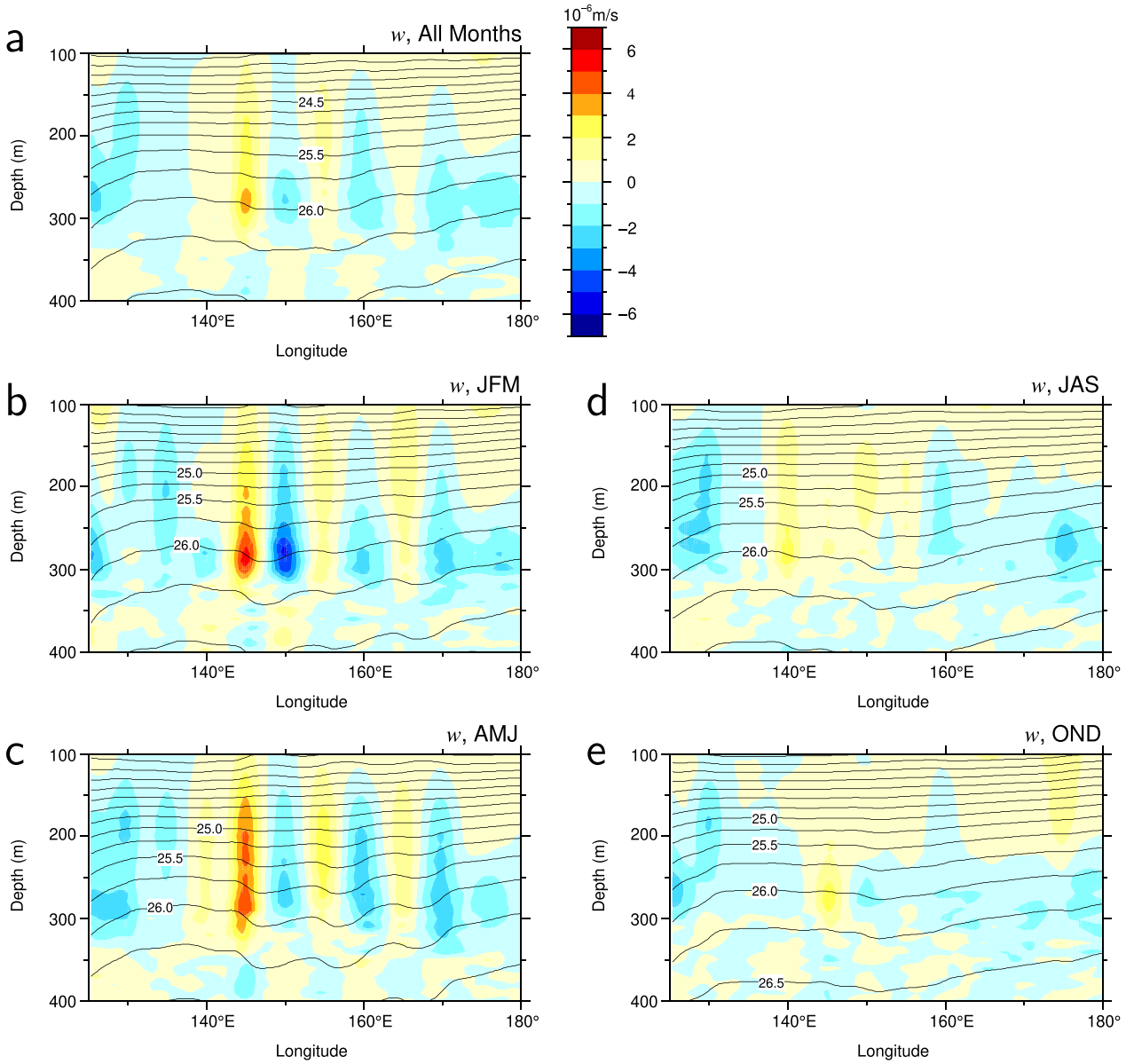

Fig. 8 Zonal sections of vertical velocity w (m s^{-1}, color shades) and potential density σ_θ (kg m^{-3}, contours) at the latitude of 12.6°N averaged in **a** all months, **b** January–March, **c** April–June, **d** July–September, and **e** October–December during 1993–2016. Positive values show upward velocity. Contour intervals of σ_θ are 0.25 kg m^{-3}

spatial scales smaller than approximately 500 km are sporadically distributed in the region south of 15°N. The spatial patterns of the vertical velocity are identifiable in the zonal and meridional sections down to a depth of 290 m, but in layers deeper than 300 m, we find noisy features with vertical scales of 10–20 m (Fig. 11c, d).

The time coefficient of the first EOF mode (black solid line in Fig. 12a) has peaks several months after peaks of the Niño 3.4 index (gray solid line), i.e., El Niño events, as in 1997–1998, 2002–2003, 2004–2005, 2009–2010, and 2015–2016. Similarly, troughs of the time coefficients are found after La Niña events such as in 1995–1996, 1998–2001, 2007–2008, and 2010–2011. The time-lagged correlation coefficient between the first EOF mode and the Niño 3.4 index shows the maximum of 0.52 with a lag of 8 months (black solid line in Fig. 13, Table 1). The maximum correlation coefficient is higher than the 5% significance level (i.e., within the 95% confidence limit) based on the Student's t test.

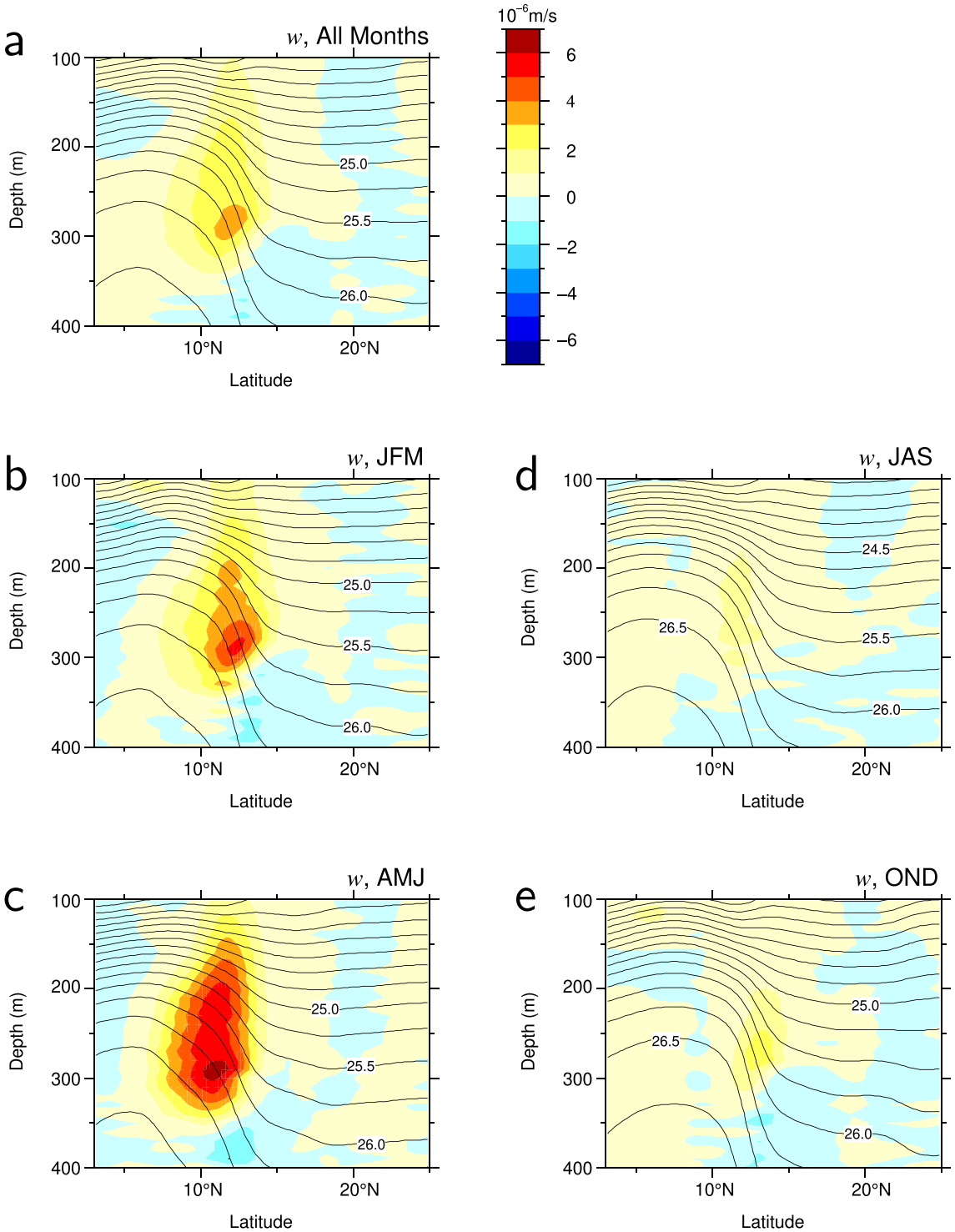

Fig. 9 Meridional sections of vertical velocity w (m s^{-1}, color shades) and potential density σ_θ (kg m^{-3}, contours) at the longitude of 145.4°E averaged in **a** all months, **b** January–March, **c** April–June, **d** July–September, and **e** October–December during 1993–2016. Positive values show upward velocity. Contour intervals of σ_θ are 0.25 kg m^{-3}

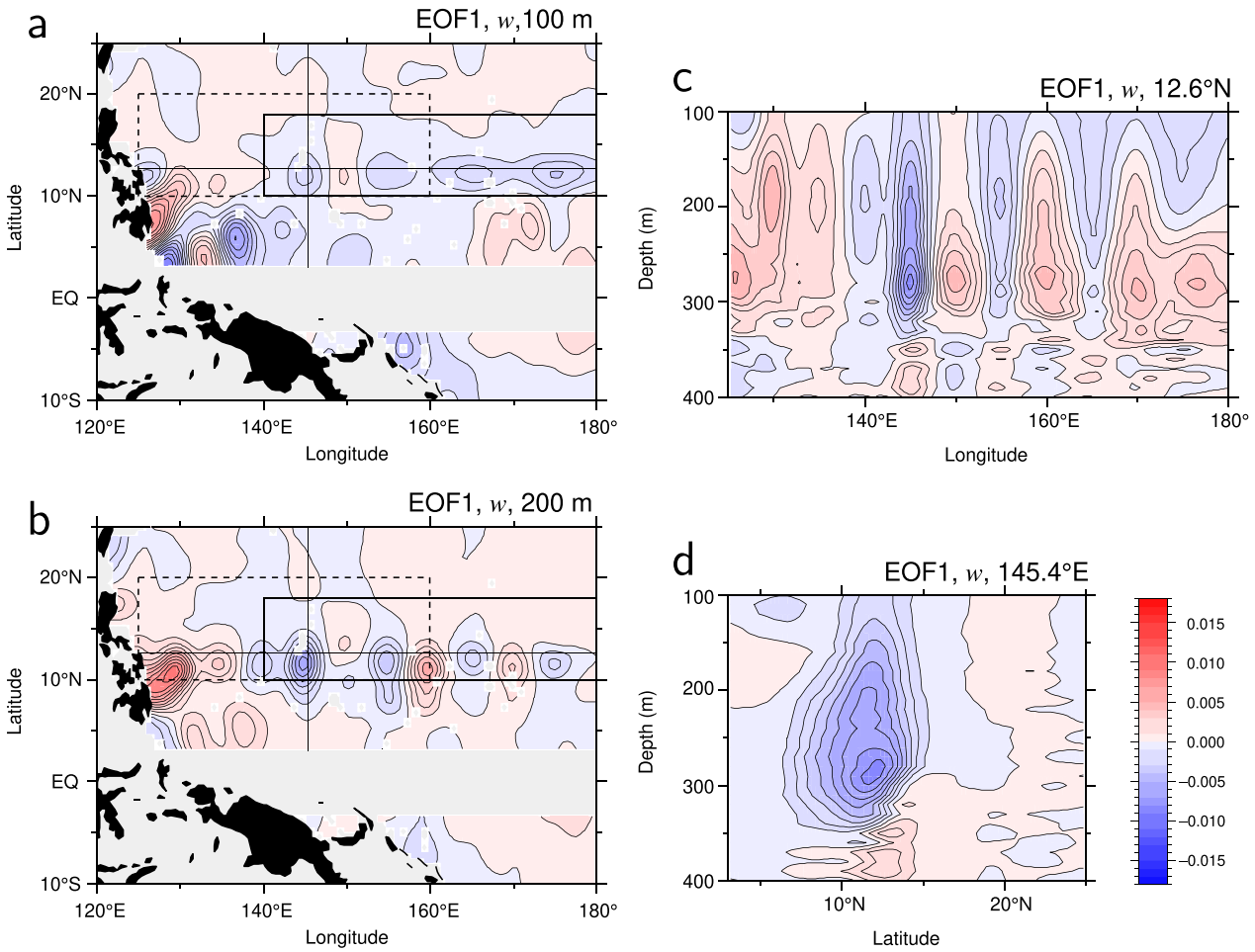

Fig. 10 First EOF mode of vertical velocity *w* in the region of 10°–25°N, 120°E–180° and the layer from 100 to 1000 m depths. The *w* data were smoothed by a 15-month running mean filter. Loadings of the EOF mode at depths of 100 m and 200 m are shown in panels **a** and **b**, respectively. Dotted square delineate the region where Nagano et al. (2016a) studied the QD variation and solid square the region (Region A) where we calculated vertical volume and temperature transports and SST tendency due to vertical current variation as in Fig. 14. Sections of the EOF mode loading at zonal 12.6°N and meridional 145.4°E lines (thin solid lines) in **a** and **b** are indicated in panels **c** and **d**, respectively. Contour intervals are 0.001

Therefore, the first EOF mode variation is significantly related to the ENSO.

Peaks of the time coefficient of the second EOF mode are found almost simultaneously with those of the Niño 3.4 index (Fig. 12b). With a lag of 1 month, the correlation coefficient reached the maximum of 0.74, which is higher than the 5% significance level and is therefore statistically significant (black dashed line in Fig. 13, Table 1). The second EOF mode variation is excited by the ENSO before the first EOF mode variation and is more highly correlated with the ENSO than the first EOF mode variation. The first EOF mode lags 9 months behind the second EOF mode with the maximum correlation coefficient of 0.71, which is much higher than the 5% significance level and is statistically significant (pink solid line in Fig. 13).

3.3 Impacts of vertical velocity variation on SST

In this subsection, we examined the impact of the interannual and longer timescale variations in the vertical velocity on the upper-ocean temperature in the region 10–17°N, 140°E–180°, referred to as Region A in what follows, where the vertical velocity at 100 m depth is prominently upward on average (shown by a solid square in Fig. 6a) and quite variable (Fig. 10a).

We calculated vertical volume transport (V_z) and temperature transport (F_z) at a depth of 100 m in Region A, which are defined as

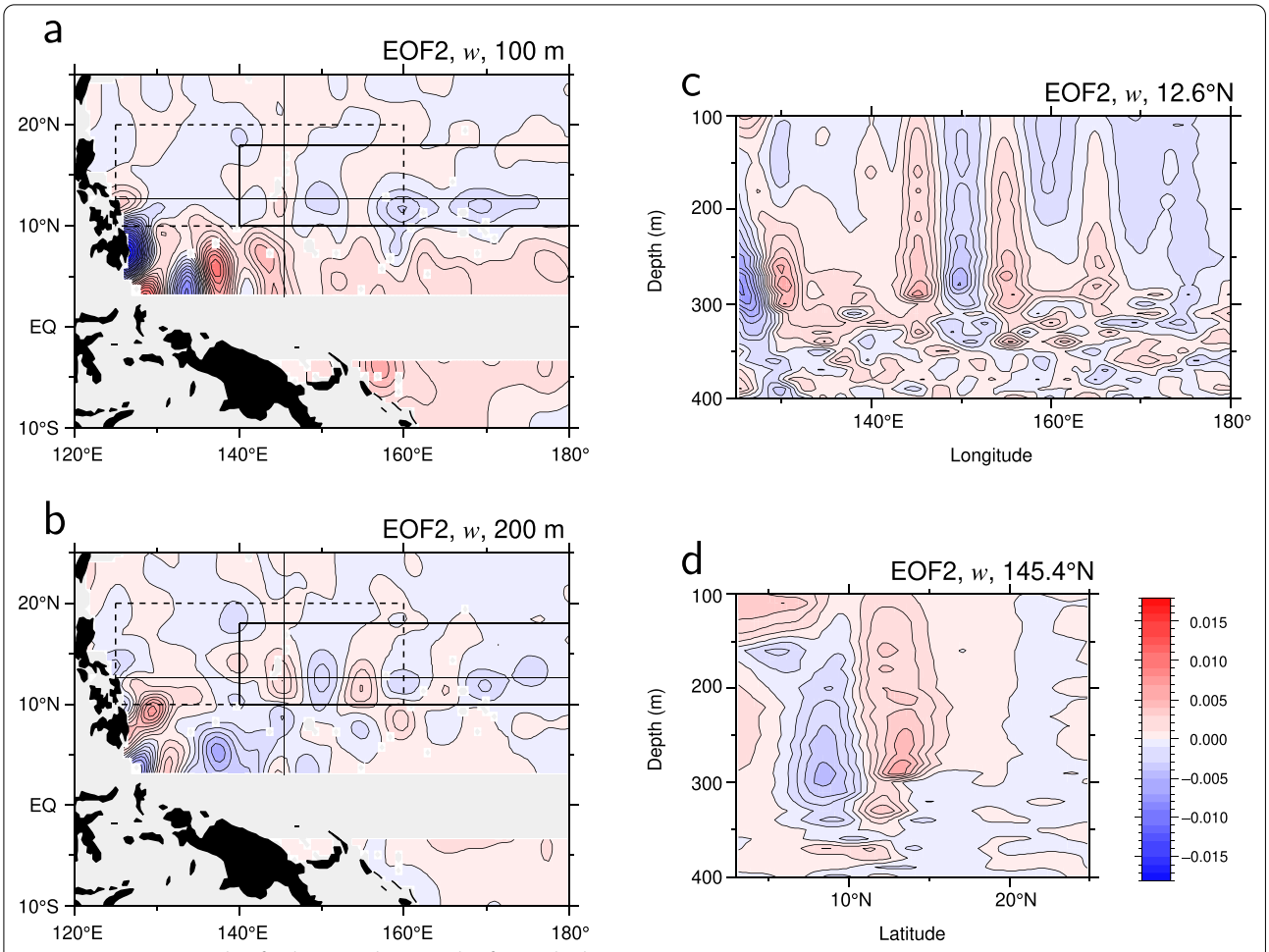

Fig. 11 Same as Fig. 10, but for the second EOF mode of vertical velocity *w*

$$V_z = \iint_{\mathrm{A}} w \, \mathrm{d}x\mathrm{d}y \tag{6}$$

and

$$F_z = \rho C_p \iint_{\mathrm{A}} \theta w \, \mathrm{d}x\mathrm{d}y, \tag{7}$$

where C_p is the specific heat capacity of seawater at constant pressure and θ is the potential temperature. ρC_p is set to $3.99\times10^6\,\mathrm{J\,K^{-1}\,m^{-3}}$.

Time series of the vertical volume and temperature transports are shown by thick black and green lines in Fig. 14a, respectively. Both modes of transports in Region A are always positive, i.e., upward, and fluctuates inversely related to the PDO and Niño 3.4 indices with correlation coefficients of −0.80 and −0.79, respectively (Table 1), being consistent with the EOF analysis in Sect. 3.2. In addition, the transport is relatively low (high) due to frequent occurrences of El Niño (La Niña) events during periods such as 1994–1998 and 2002–2005 (1999–2001 and 2007–2014). This relationship is clearly shown by the QD component of the Niño 3.4 index smoothed by a 37-month running mean filter (Hasegawa et al. 2013) (thin magenta line in Fig. 14a), which is inversely related to the vertical volume transport (thin black line in Fig. 14a).

When the volume transport reached the maximum over 1.5 Sv in summer (July) of the 2008 La Niña year (downward arrow in Fig. 14a), the upward current velocity exceeded $1\times10^{-6}\,\mathrm{m\,s^{-1}}$ in the region from 150°E to 180° around 12°N (Fig. 15b). The strong upwelling was driven principally by the southward current greater than 1 $\mathrm{cm\,s^{-1}}$ at 100 m depth (contours in Fig. 15b) existing above the isopycnal zone of 25.0–25.5 σ_θ at 200 m depth (vertical line mesh), which impinged on the slope of the isopycnals shoaling southward. In this period, the southward current in the isopycnal layer of 25.0–25.5 σ_θ was mostly distributed in the

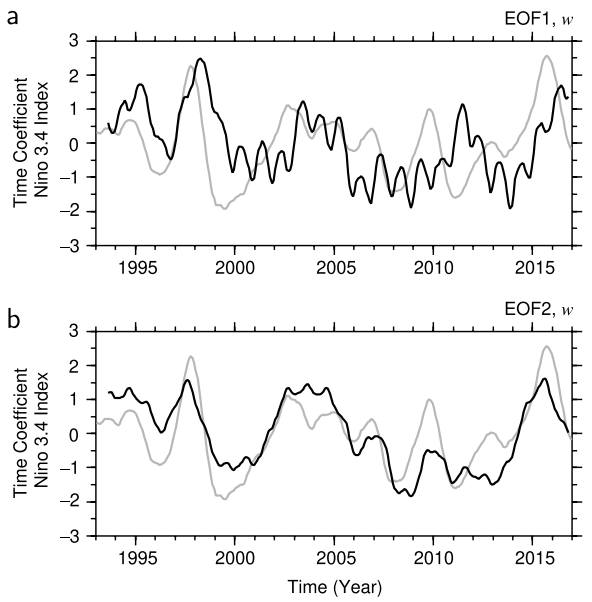

Fig. 12 Time coefficients of the **a** first and **b** second EOF modes of vertical velocity *w* (black lines) and Niño 3.4 index (gray lines). For comparison, Niño 3.4 index was smoothed by a 15-month running mean filter. All the time series were normalized by their standard deviations

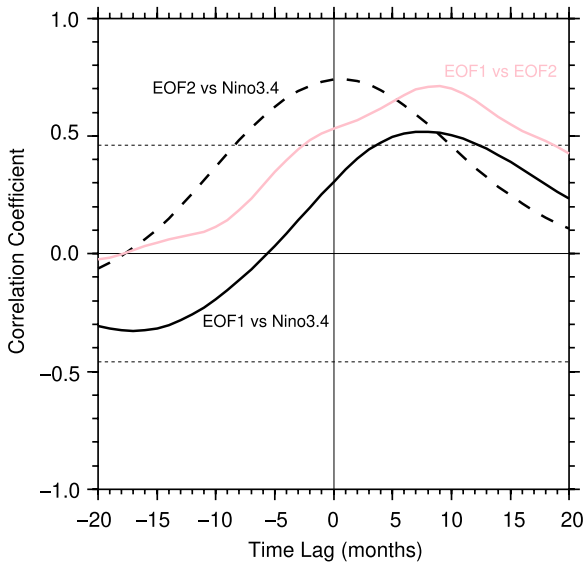

Fig. 13 Time-lagged correlation coefficients of the first (black solid line) and second (black dashed line) EOF modes of vertical velocity *w* with respect to Niño 3.4 index and that between the first and second EOF modes (pink solid line). The time series were smoothed by a 15-month running mean filter. The positive time lag with respect to Niño 3.4 index indicates that the EOF modes of vertical velocity lag the Niño 3.4 index. The positive time lag between the EOF modes denotes that the first mode lags the second mode. The vertical solid line denotes the zero time lag. The horizontal dotted and solid lines show the 95% confidence interval (±0.46) and zero correlation, respectively

subtropical gyre interior region (10°–25°N, 145°E–180°) (Fig. 16b). The westward velocity of the NEC in this isopycnal layer was higher than 15 cm s^{-1} to the east of 160°E.

Meanwhile, in the summer (July) of the 1997 El Niño year (upward arrow in Fig. 14a), the vertical velocity in Region A was weakly upward or downward, and the corresponding southward current was observed only in a limited region centered around 14°N, 175°E (Fig. 15a). The area of the subtropical gyre interior southward current in the isopycnal layer of 25.0–25.5 σ_θ and the intensity of the NEC are both smaller than those in the 2008 summer (Fig. 16a). The QD variations in the vertical velocity just beneath a depth of 100 m are expected to contribute to the QD variation in SST in the western tropical North Pacific related to the PDO as illustrated in Fig. 1.

Because the water temperature and vertical velocity at 100 m depth are not horizontally uniform, the temperature of upwelling water is not necessarily identical to the area-averaged temperature within Region A. The water temperature of water mass transported by the vertical current can be examined by the volume transport-weighted temperature (Θ) at a depth of 100 m defined as

Table 1 Correlation coefficients of the first and second EOF mode time coefficients of vertical velocity *w*, vertical volume transport (V_z), and vertical temperature transport (F_z) at 100 m depth with respect to Niño 3.4 index; and those of V_z, F_z, the temperature tendency ($\partial T_w/\partial t$) and temperature variation (T'_w) in the top 100 m layer in Region A with respect to PDO index

Climate index	*w*-related variable	Correlation coefficient	Time lag (months)
Niño 3.4	EOF1_*w*	0.52	8
	EOF2_*w*	0.74	1
	V_z,	−0.79	0
	F_z	−0.79	0
PDO	V_z	−0.80	0
	F_z	−0.80	0
	$\partial T_w/\partial t$	0.63	0
	T'_w	−0.65	−34

Positive time lag indicates that the *w*-related variables lag behind the climate index

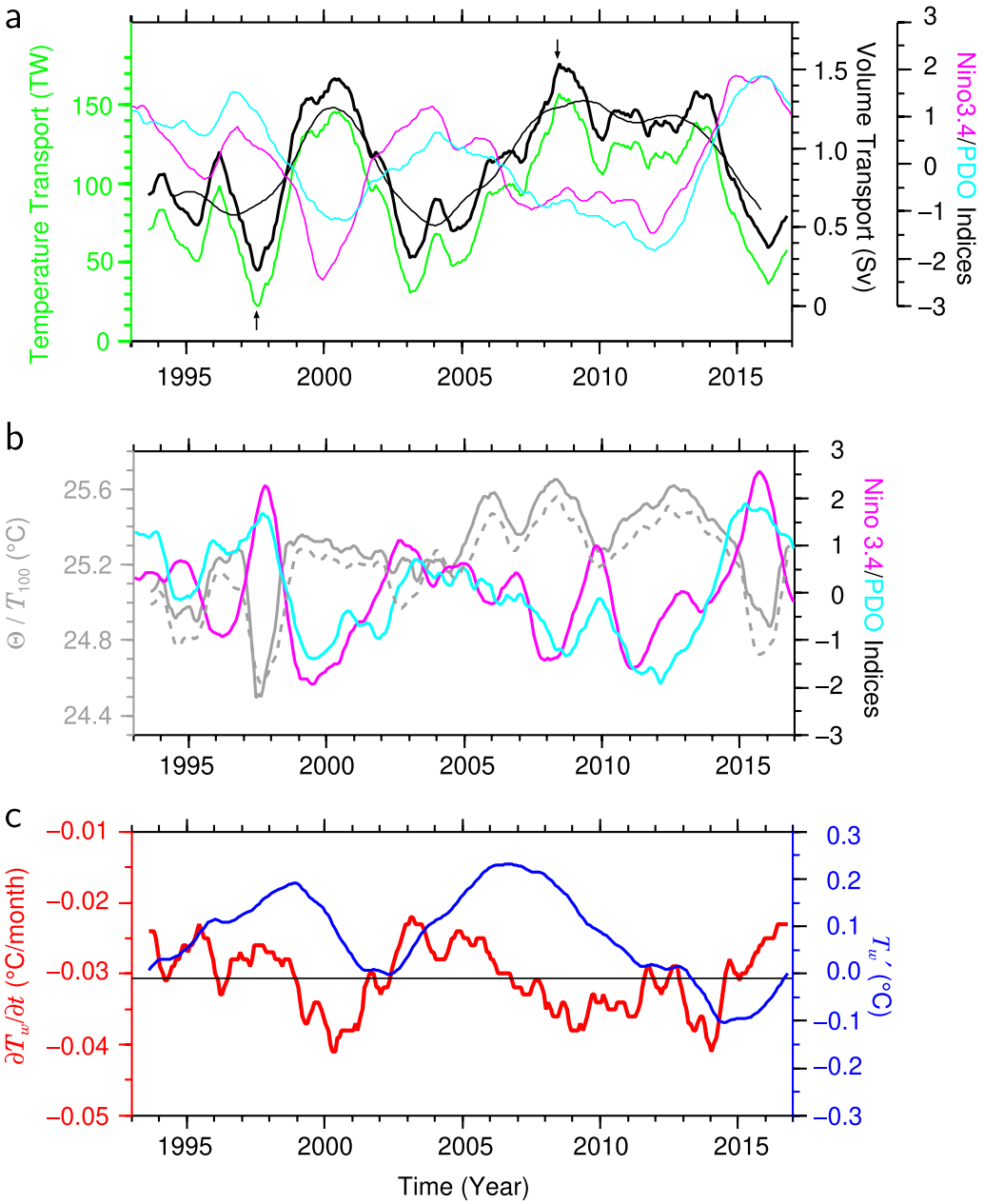

Fig. 14 **a** Volume transport V_z (Sv, thick black line) and temperature transport F_z (TW, green line) at 100 m depth in Region A shown by the solid square in Figs. 6, 7, 10, and 11. V_z, Niño 3.4, and PDO indices smoothed by a 37-month running mean filter are shown by thin black, magenta, and cyan lines, respectively. Upward and downward arrows indicate July 1997 and July 2008, respectively. **b** Volume transport-weighted temperature Θ (°C, gray solid line) and area-averaged temperature T_{100} (°C, gray dashed line) at 100 m depth and Niño 3.4 (magenta line) and PDO (cyan line) indices. **c** Upper-ocean (< 100 m depth) temperature tendency, $\partial T_w/\partial t$, averaged in Region A (°C month^{-1}, red line) and temperature variation, T_w', (°C, blue line) in the top 100 m layer. The horizontal black thin line indicates the mean value of the upper-ocean temperature tendency (−0.031°C month^{-1}). The climate indices in panels **a** and **b** were normalized by the standard deviations

$$\Theta = \frac{F_z}{\rho C_p V_z}. \tag{8}$$

The volume transport-weighted temperature (gray solid line in Fig. 14b) varies on the QD timescale in opposite phase with the Niño 3.4 index (magenta line in Fig. 14b) because of the anomalously warm (cold) water in the upper layer of the western Pacific warm pool in La Niña (El Niño). Therefore, the increase in Θ just below a depth of 100 m in La Niña years acts to reduce the cooling effect

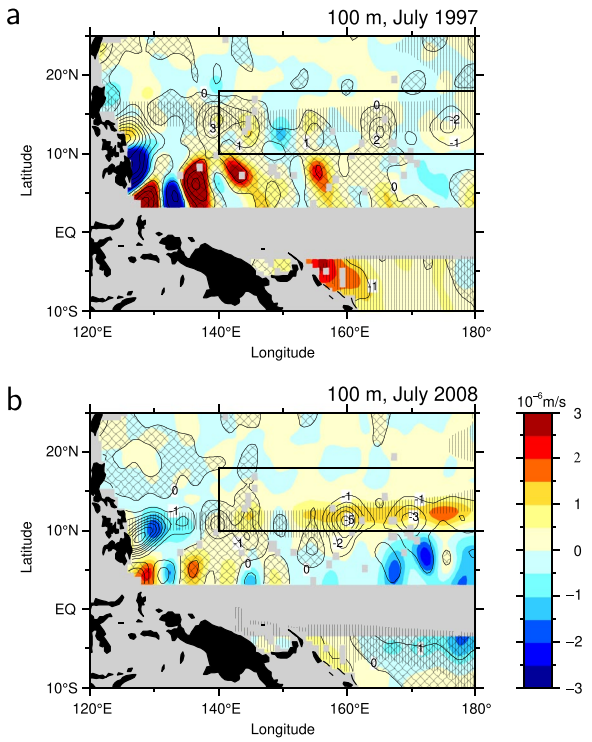

Fig. 15 Horizontal distributions of smoothed upward velocity w (m s^{-1}, color shading) and northward velocity v (cm s^{-1}, contours) at a depth of 100 m in **a** July 1997 and **b** July 2008, i.e., periods of the weak and strong upward transports in Region A (solid square), which are denoted by upward and downward arrows in Fig. 14a, respectively. Data were smoothed by a 15-month running mean filter. Contour intervals of v are 1 cm s^{-1} and cross line meshing indicates northward velocity. Vertical line meshing illustrates the isopycnal zone of at a depth of 200 m

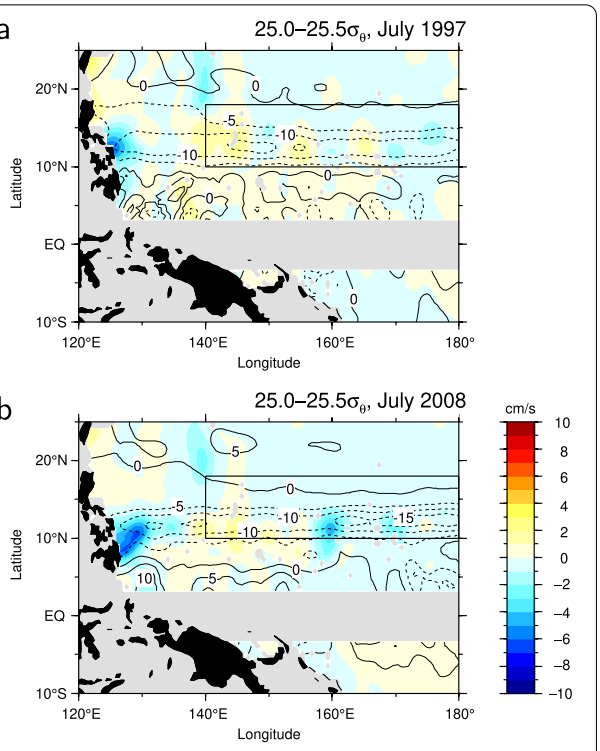

Fig. 16 Distributions of eastward velocity u (cm s^{-1}, contours) and northward velocity v (cm s^{-1}, color shading) averaged within isopycnal layers of 25.0 and 25.5 σ_θ in **a** July 1997 and **b** July 2008, i.e., periods of the weak and strong upward transports in Region A (solid square), which are denoted by upward and downward arrows in Fig. 14a, respectively. Data were smoothed by a 15-month running mean filter. Contour intervals of u are 5 cm s^{-1} and dashed contours indicate negative values (westward velocity)

of the enhancement of the upward velocity. Because of the nonuniformity of w, Θ is approximately 0.1 °C higher than the area-averaged temperature, T_{100} (gray dashed line in Fig. 14b). However, note that, as will be shown below, the volume transport-weighted temperature variation is much less effective in the upper-ocean temperature variation than the upward current variation.

The upward volume and temperature transports in Region A decrease with the depth because, in layers deeper than 150 m, upward currents are compensated by similar magnitude downward currents (Fig. 8). For example, the volume and temperature transports at 200 m depth are mostly positive (upward) but smaller than 0.8 Sv and 50 TW, respectively. Their correlation coefficients with respect to the Niño 3.4 index are −0.44, absolute values of which are smaller than the 5% significance level.

To examine the impact of the vertical velocity and temperature variations at 100 m depth on the temperature in the overlying layer, we estimate temperature tendency ($\partial T_w/\partial t$) averaged in the top 100 m due to the vertical velocity variation, w, i.e., vertical advection of temperature ($w\partial T/\partial z$), by the following formula:

$$\frac{\partial T_w}{\partial t} = -\frac{w(T_\mathrm{u} - T_\mathrm{d})}{h_\mathrm{u}}, \tag{9}$$

where h_u is the depth of the uppermost level of the estimation of w (i.e., 100 m), T_d is the potential temperature just below 100 m depth, and T_u is the upper-ocean (< 100 m depth) temperature. T_d and T_u are set to the AGEM-derived potential temperature at the 110 m depth and monthly gridded value of SST prepared by Reynolds et al. (2002), respectively. We assigned to w the time-varying vertical velocity at a depth of 100 m derived from the P-vector inverse method. When the vertical velocity is negative (or downward), w is set to zero, i.e., $w = 0$.

The temperature tendency, $\partial T_w/\partial t$, based on Eq. (9) and averaged in Region A is shown in Fig. 14c. The QD variability (red line in Fig. 14c) is remarkable and is almost in phase with the PDO index (cyan line in Fig. 14b) with

a significant correlation coefficient of 0.63 (Table 1). Associated with the enhancement of the vertical volume transport (Fig. 14a), the temperature tendency has substantial troughs in 2000, 2009, and 2014, which occur 6–8 years after the peaks of the volume transport in the isopycnal layer between 25.0 and 25.5 σ_θ in the subtropical gyre interior region in 1994, 2001, and 2006 estimated by Nagano et al. (2016a). The minimum value of the temperature tendency (-0.04 °C month^{-1}) in the spring of 2000 is approximately 30% of the annual mean cooling rates of the mixed layer due to the vertical entrainment and the net surface heat flux, which were individually estimated to be approximately -0.13 °C month^{-1} by Qu (2003); thus, the variation in the upward advection of the deep cold water due to the vertical velocity variation has a critical influence on the QD upper-ocean temperature variation.

4 Discussion

4.1 Relation of the upward current cooling to the PDO

The temperature variation obtained by temporally integrating the anomaly of $\partial T_w/\partial t$, i.e., $T'_w = \int \partial T'_w/\partial t \, \mathrm{d}t$, exhibits a smooth QD variation with peaks in 1999 and 2006 (blue line in Fig. 14c). These peaks largely coincide with those of the QD SST variation in the North Pacific warm pool region calculated by Nagano et al. (2016a) in the region marked by the dotted square (Figs. 6, 7, 10a, 11a) and the troughs of the QD variation in the net heat transport examined by Nagano et al. (2016a). The peak values of T'_w reach or exceed 0.2 °C, which is equivalent to the regression slope in the western tropical North Pacific with a lag of 3 years as illustrated in Fig. 1d. T'_w inversely varies leading 34 months to the PDO index with a significant correlation coefficient of -0.65 (Table 1). The leading time (34 months) is a little longer than a leading time (2 years) of the variation in coral nitrogen isotope concentrations in Tatsukushi Bay, Japan, a possible proxy for the surface Kuroshio water temperature, to the PDO index reported based on 36-year time series by Yamazaki et al. (2016). The discrepancy (8 months) between the time leads of this study and that of Yamazaki et al. (2016) can be explained by the advection time of approximately 9 months evaluated by Nagano et al. (2014, 2017) from the northward propagation of sea surface salinity variation along the western subtropical North Pacific.

Therefore, 6–8 years after the variation in the volume transport in the isopycnal layer of 25.0–25.5 σ_θ in the subtropical gyre (Nagano et al. 2016a), the vertical volume transport in the region east of the Philippines (10°–17°N, 140°E–180°) changes and it modifies the upper-ocean temperature through the vertical advection of the cold deep water to the upper ocean. Considering the horizontal advection time scale of water masses in the subtropical gyre interior region (∼10 years) (e.g., Sasaki et al. 2010), the time lag between the variations in the vertical volume transport to the east of the Philippines and the volume transport in an isopycnal layer of 25.0–25.5 σ_θ (6–8 years) appears to be reasonable.

The relations of the upwelling strength in the NEC to the positive and negative phases of the PDO are summarized in Fig. 17a, b, respectively. In the positive phase of the PDO, the subtropical gyre interior flow in the isopycnal layer between 25.0 and 25.5 σ_θ is strengthened (Fig. 17a). The strengthened interior flow disturbance proceeds southwestward and, 6–8 years after, reaches the east of the Philippines, and cools the upper ocean in the western tropical North Pacific (Fig. 17b), leading to the negative phase of the PDO.

The excessive accumulated heat in the western tropical North Pacific during approximately 4 years by the attenuation of the vertical velocity is considered to be advected northward by the Kuroshio (Fig. 17a) as inferred from the extension of the positive regression slope (high SST after the positive PDO phase) in the western subtropical Pacific (Fig. 1d). Note that the high SST anomaly is attributable not to the positive PDO phase 3–4 years before but to the negative PDO phase approximately 10 years before. The anomalously warm water is transported to the midlatitude region of the North Pacific by the Kuroshio and the Kuroshio Extension, yielding the next negative phase of the PDO. The strengthening (weakening) of the upward transport in Region A in the negative (positive) phase of the PDO is critically related to the reversal of the PDO phase. Note that, in the region east of the Philippines, there are mixed layer depth and barrier layer thickness variations (Sato et al. 2004; Nagano et al. 2018), which may change responses of SST to the surface heat flux and vertical current variations but cannot be accounted in this study. In particular, it is unclear how the barrier layer thickness varies and affects the SST variation. Future comprehensive studies are necessary to better understand the SST variation in the western North Pacific related to the reversal of the PDO phase.

4.2 Effect of vertical eddy diffusion

The upward transport in Region A can be attributed to both the adiabatic and diabatic processes. The adiabatic process contributes to the upward transport through the upward displacement of the main pycnocline (around 10°N latitude) associated with the intensification of the northern part of the NEC. On the other hand, the isopycnal layer of 25.0–25.5 σ_θ, where Nagano et al. (2016a) found the QD volume transport variation in the subtropical gyre interior region, does not reach the mixed layer

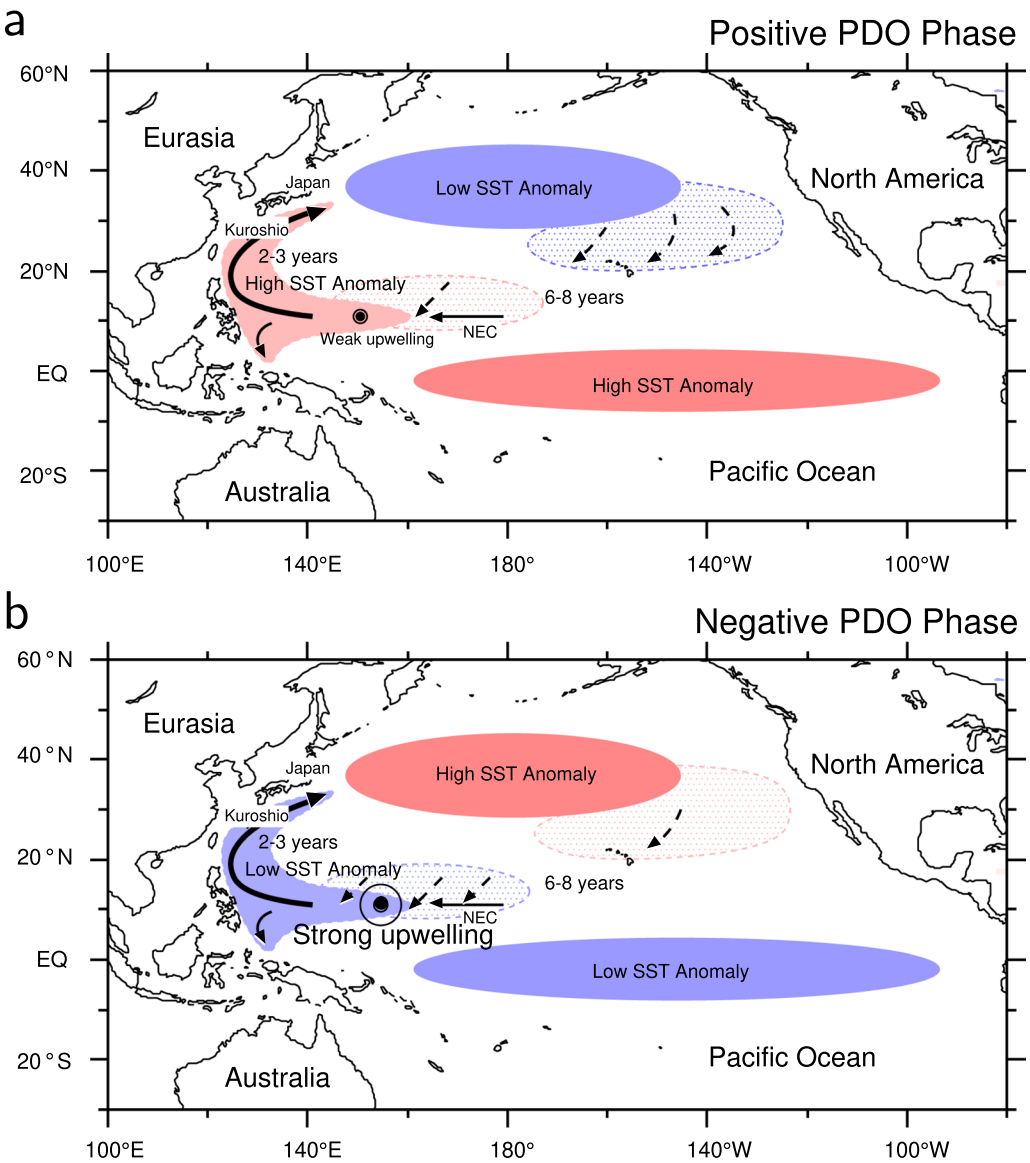

Fig. 17 Schematic representation of the upwelling strength in the NEC region and temperature anomalies in the **a** positive and **b** negative PDO phases. SST anomalies are denoted by solid shades and subsurface temperature anomalies dotted shades. High and low temperature anomalies are colored red and blue, respectively. The sea surface Kuroshio and Mindanao currents are illustrated by solid arrows and the subsurface subtropical gyre interior currents dashed arrows

base (< 100 m depth) (de Boyer Montégut et al. 2004) in Region A, although the upward velocity in this region extends from 250 to 100 m in all seasons (Figs. 8, 9). The mechanism of the water mass transport across the isopycnal surfaces, i.e., the diabatic process, is considered to be of importance in the process that the subsurface water-mass volume fluctuations are entrained into the sea surface mixed layer.

In this subsection, we examine whether or not the eddy diffusive mechanism is important, by estimating the order of the magnitude of diapycnal eddy diffusivity from the AGEM potential density and vertical velocity. Assuming that the vertical advection is balanced with the diapycnal diffusion:

$$w\frac{\partial \rho}{\partial z} = K_\rho \frac{\partial^2 \rho}{\partial z^2},$$

where K_ρ is diapycnal eddy diffusivity (e.g., Pedlosky 1987b), we can estimate K_ρ. On the basis of the AGEM-based potential density, we set $\partial\rho/\partial z$ and $\partial^2\rho/\partial z^2$ to

1.0×10^{-2} kg m^{-4} and 1.0×10^{-4} kg m^{-5}, respectively, and for $w = 1.0 \times 10^{-6}$ m s^{-1}, K_ρ is estimated to be 1.0×10^{-4} m^2 s^{-1}. Considering that the isopycnals can move adiabatically in the real ocean, this value is considered to be the upper limit of the diffusivity that should be observed.

Whalen et al. (2012) estimated global distribution of diapycnal eddy diffusivity based on Argo hydrographic data obtained in the period from 2006 to 2011, during which La Niña events frequently occurred. The estimated value of K_ρ in the present study is of the same order of magnitude as globally averaged diffusivity at a depth of 200 m (Fig. S.5a of Whalen et al. 2012) calculated by Whalen et al. (2012). Note that the vertical transports are relatively large (black and green lines in Fig. 14a) in Whalen et al.'s study period (2011–2016). There exists noticeably enhanced diffusivity in a layer from 250 to 500 m depths over the rough ocean bottom in the western tropical North Pacific (Figs. 2a and S.1 of Whalen et al. 2012), which covers Region A. Even though the diapycnal process is not accounted for in the P-vector inverse method, the enhancement of the eddy diffusivity in La Niña condition by the rough bottom topography is consistent with the La Niña-related strengthening of the vertical velocity estimated in this study. Future observations of vertical eddy diffusion by microstructure profilers in addition to CTD data in both phases of the ENSO may be useful to clarify the relationship between the vertical velocity in Region A and the bottom topography.

4.3 Vertical currents by the Ekman current divergence near sea surface

Note that the vertical currents near the sea surface cannot be studied by the P-vector method because they are considered to be strongly affected by the Ekman currents. Near the sea surface in the tropical (south of 13°N) and subtropical (north of 13°N) western North Pacific, the wind-driven Ekman currents are divergent and convergent, causing upwelling and downwelling, respectively (e.g., Fig. 7 of Tozuka et al. 2002). The upward velocity induced by the Ekman currents is particularly strong in winter and reaches the order of 10^{-6} m s^{-1}. Although the thickness of the Ekman layer is approximately 20 m even in the tropical North Pacific (Fig. 4 of Ralph and Niiler 1999), which is remarkably less than 100 m depth, the upward current at 100 m depth in the western tropical region may be strengthened by the Ekman upwelling.

5 Conclusions

Prior to the negative (positive) phase of the PDO, the SST in the western tropical North Pacific is heated (cooled). The SST variation is suggested to be related to the QD-timescale (8–12 years) variation in the volume transport in the subsurface layer of 25.0–25.5 σ_θ (Nagano et al. 2016a). To reveal where the QD variation in the volume transport in the subsurface layer emerges in the western tropical North Pacific and how great the impact of the variation on the upper-ocean temperature is, we examined the spatiotemporal characteristics of the 3D field of vertical velocity. By the area-wise AGEM method, we estimated 3D potential temperature and salinity fields in the region of 10°S–25°N, 120°E–180° during the period from January 2001 to May 2017 using altimetric SSH data and CTD profile data collected by Argo floats. The 3D potential density field was computed from the AGEM-derived potential temperature and salinity. The streamfunction in the top 1000 dbar calculated from the AGEM-derived potential density is consistent with previous studies.

Applying the P-vector inverse method to the 3D AGEM-derived potential density field, we obtained the time-varying 3D vertical velocity field. Vertical velocity is observed in a layer down to a depth of approximately 350 m. Associated with the seasonal westward shrinkage of the MD in boreal winter and spring, the westward flowing NEC approaches to the NECC and wavy patterns of the streamfunction and corresponding vertical velocity fluctuations are generated between the currents possibly through the barotropic instability due to the enhanced horizontal shear. Furthermore, the regional-scale upward current was found in the NEC, 10°–17°N, 140°E–180°, called Region A in this paper. In this region, the southward shoaling of the isopycnal surfaces between 25.0 and 26.5 σ_θ produces a mean substantial upward velocity of approximately 1×10^{-6} m s^{-1} at a depth of 100 m depth. Possibly in addition to the Ekman upwelling in the western tropical North Pacific, the upward current driven by the southward current impinged on the isopycnal slope advects the deep cold water to the upper ocean.

To examine the spatiotemporal characteristics, the interannual to decadal variations in the vertical velocity were decomposed by the EOFs. The first and second EOF modes represent the ENSO-timescale enhancement (attenuation) of the upward velocity at 100 m depth in the region of 10°–17°N, 140°E–180° (Region A) with peaks approximately 8 and 1 months after La Niña (El Niño) events, explaining 66% and 11% of the total variance, respectively. Furthermore, due to frequent occurrences of La Niña (El Niño) events, the upward velocity was observed to vary on the longer timescale, i.e., the QD timescale. The volume and temperature transports of the vertical velocity in the region of 10°–17°N, 140°E–180° vary on the QD timescale. The maxima of the volume and temperature transports are estimated to be approximately 1.5 Sv and 150 TW in the La Niña year of 2008, respectively. At this time, the upward current reached the

maximum exceeding 1×10^{-6} m s^{-1} in Region A, being forced by the southward current greater than 1 cm s^{-1} impinged on the sloping isopycnal surfaces.

The cooling effect of the upper ocean (< 100 m depth) due to the upward current advection was examined. The attenuation (intensification) of the upward transport in the positive (negative) phase of the PDO keeps the upper-ocean temperature tendency, i.e., temporal change in the temperature, anomalously high (low) approximately 6–8 years after the decrease (increase) in the volume transport in an isopycnal layer of 25.0–25.5 σ_θ in the subtropical gyre interior region, as reported by Nagano et al. (2016a), and increase (decrease) SST in the western tropical North Pacific, as schematically illustrated, respectively, for the positive and negative PDO phases in Fig. 17. The decreases in the vertical volume transport cause the upper-ocean temperature increase by 0.2 °C or greater, which is equivalent to the SST change associated with the PDO. The QD variation in the vertical velocity in Region A can be critically related to the reversal of the PDO phase through the heat transport of the Kuroshio. This result, as well as atmospheric teleconnections from the tropical region (Alexander et al. 2002), suggests that there is a significant oceanic link connecting the mid- and high-latitude regions to the tropical region.

Abbreviations

3D: Three-dimensional; AGEM: Altimetry-based gravest empirical mode; CTD: Conductivity–temperature–depth; ENSO: El Niño-Southern Oscillation; EOF: Empirical orthogonal function; MOAA GPV: Grid point value of the Monthly Objective Analysis using the Argo; MD: Mindanao Dome; NEC: North Equatorial Current; NECC: North Equatorial Countercurrent; NOAA: US National Oceanic and Atmospheric Administration; PDO: Pacific decadal oscillation; QD: Quasi-decadal; RMS: Root mean square; SSH: Sea surface height; SST: Sea surface temperature.

Acknowledgements

The 3D hydrographic field estimation by the AGEM method applying to Argo profile data owes a lot to discussion with Prof. Kimio Hanawa and Prof. Shoichi Kizu (Tohoku University). The authors are grateful to the editors, Dr. Michio Kawamiya (JAMSTEC) and Prof. Eiji Ohtani (Tohoku University), and anonymous reviewers for constructive review comments.

Author contributions

TH currently belongs to Japan Meteorological Agency. He contributed to this study when he belonged to Tohoku University and Hokkaido University. AN proposed the topic, conceived, designed the study, analyzed the data, and constructed the manuscript. TH analyzed the data and collaborated with the corresponding author (AN) in the construction of manuscript. MW discussed the results in cooperation with AN and TH. All authors read and approved the final manuscript.

Funding

This work was partly supported by the Japan Society for the Promotion of Science, Grant-in-Aid for Scientific Research (Grant Nos. JP15H04228, JP17K05660, JP20K04072, JP20H02236, JP20H04349, JP20KK0097).

Availability of data and materials

Quality-controlled Argo profile data (Advanced automatic QC Argo Data version 1.2) were provided in the Japan Argo database (ftp://ftp2.jamstec.go.jp/pub/argo/). Daily altimetric SSH data and monthly NOAA Optimum Interpolation SST V2 data were produced by the EU Copernicus Marine Environment Monitoring Service (CMEMS) (ftp://my.cmems-du.eu/) and the US NOAA/OAR/ESRL (https://psl.noaa.gov/data/gridded/data.noaa.oisst.v2.html).

Declarations

Competing interests

The authors declare that they have no competing interest.

Author details

[1]Center for Coupled Ocean-Atmosphere Research (CCOAR), Japan Agency for Marine-Earth Science and Technology (JAMSTEC), 2-15 Natsushima-cho, Yokosuka, Kanagawa 237-0061, Japan. [2]Faculty of Environmental Earth Science, Hokkaido University, N10-W5 Kita-ku, Sapporo, Hokkaido 060-0810, Japan. [3]Graduate School of Science, Tohoku University, 6-3 Aoba Aramaki-aza Aoba-ku, Sendai, Miyagi 980-8578, Japan. [4]Mutsu Institute for Oceanography (MIO), Japan Agency for Marine-Earth Science and Technology (JAMSTEC), 690 Kitasekine Sekine, Mutsu, Aomori 035-0022, Japan.

Received: 24 June 2022 Accepted: 29 September 2022
Published online: 22 October 2022

References

Akima H (1970) A new method of interpolation and smooth curve fitting based on local procedures. J Assoc Comput Mach 17:589–602
Alexander MA, Bladé I, Newman M, Lanzante JR, Lau N-C, Scott JD (2002) The atmospheric bridge: the influence of ENSO teleconnections on air-sea interaction over the global oceans. J Clim 15:2205–2231
Anderberg MR (1973) Cluster analysis for applications: probability and mathematical statistics. Academic Press, New York
Bryden HL, Imawaki S (2001) Ocean heat transport. In: Siedler H, Church J, Gould J (eds) Ocean circulation and climate: observing and modeling the global ocean. Academic Press, London, pp 455–474
Chu PC (1995) P-vector method for determining absolute velocity from hydrographic data. Mar Technol Soc J 29(3):3–14
Chu PC (2006) P-vector inverse method. Springer, Berlin. https://doi.org/10.1007/978-3-540-33386-9
de Boyer Montégut C, Madec G, Fischer AS, Lazar A, Iudicone D (2004) Mixed layer depth over the global ocean: an examination of profile data and a profile-based climatology. J Geophys Res. https://doi.org/10.1029/2004JC002378
Deser C, Alexander MA, Timlin MS (1996) Upper-ocean thermal variations in the North Pacific during 1970–1991. J Clim 9:1840–1855
Fine RA, Lukas R, Bingham FM, Warner MJ, Gammon RH (1994) The western equatorial Pacific: a water mass crossroads. J Geophys Res 99(C12):25063–25080. https://doi.org/10.1029/94JC02277
Flament P (2002) A state variable for characterizing water masses and their diffusive stability: spiciness. Prog Oceanogr 54:493–501
Gill AE (1982) Atmosphere-ocean dynamics. Academic Press, London
Gu D, Philander SGH (1997) Interdecadal climate fluctuations that depend on exchange between the tropics and extratropics. Science 275:805–807. https://doi.org/10.1126/science.275.5301.805
Hasegawa T, Hanawa K (2003) Decadal-scale variability of upper ocean heat content in the tropical Pacific. Geophys Res Lett. https://doi.org/10.1029/2002GL016843
Hasegawa T, Ando K, Ueki I, Mizuno K, Hosoda S (2013) Upper-ocean salinity variability in the tropical Pacific: case study for quasi-decadal shift during the 2000s using TRITON buoys and Argo floats. J Clim 26:8126–8138. https://doi.org/10.1175/JCLI-D-12-00187.1
Hosoda S, Ohira T, Nakamura T (2008) A monthly mean dataset of global oceanic temperature and salinity derived from Argo float observations. JAMSTEC Rep Res Dev 8:47–59
Kashino Y, Ishida A, Hosoda S (2011) Observed ocean variability in the Mindanao Dome region. J Phys Oceanogr 41:287–302. https://doi.org/10.1175/2010JPO4329.1
Kawai Y, Doi T, Tomita H, Sasaki H (2008) Decadal-scale changes in meridional heat transport across 24°N in the Pacific Ocean. J Geophys Res. https://doi.org/10.1029/2007JC004525

Killworth PD (1983) Absolute velocity calculations from single hydrographic sections. Deep-Sea Res 30(5A):513–542
Killworth PD (1986) A Bernoulli inverse method for determining the ocean circulation. J Phys Oceanogr 16:2031–2051
Latif M, Barnett TP (1994) Causes of decadal climate variability over the North Pacific and North America. Science 266:634–637
Latif M, Barnett TP (1996) Decadal climate variability over the North Pacific and North America: dynamics and predictability. J Clim 9:2407–2423
Mantua NJ, Hare SR (2002) The Pacific decadal oscillation. J Oceanogr 58:35–44
Mantua NJ, Hare SR, Zhang Y, Wallace JM, Francis RC (1997) A Pacific interdecadal climate oscillation with impacts on salmon production. Bull Am Meteorol Soc 78(78):1069–1079
Nagano A, Ichikawa K, Ichikawa H, Konda M, Murakami K (2009) Synoptic flow structures in the confluence region of the Kuroshio and the Ryukyu Current. J Geophys Res. https://doi.org/10.1029/2008JC005213
Nagano A, Ichikawa K, Ichikawa H, Tomita H, Tokinaga H, Konda M (2010) Stable volume and heat transports of the North Pacific subtropical gyre revealed by identifying the Kuroshio in synoptic hydrography south of Japan. J Geophys Res. https://doi.org/10.1029/2009JC005747
Nagano A, Ichikawa H, Yoshikawa Y, Kizu S, Hanawa K (2012) Variation of the southward interior flow of the North Pacific subtropical gyre, as revealed by a repeat hydrographic survey. J Oceanogr 68(2):361–368. https://doi.org/10.1007/s10872-012-0102-3
Nagano A, Uehara K, Suga T, Kawai Y, Ichikawa H, Cronin MF (2014) Origin of near-surface high-salinity water observed in the Kuroshio Extension region. J Oceanogr 70:389–403. https://doi.org/10.1007/s10872-014-0237-5
Nagano A, Kizu S, Hanawa K, Roemmich D (2016a) Heat transport variation due to change of North Pacific subtropical gyre interior flow during 1993–2012. Ocean Dyn 66(12):1637–1649. https://doi.org/10.1007/s10236-016-1007-2
Nagano A, Wakita M, Watanabe S (2016b) Dichothermal layer deepening in relation with halocline depth change associated with northward shrinkage of North Pacific western subarctic gyre in early 2000s. Ocean Dyn 66(2):163–172. https://doi.org/10.1007/s10236-015-0917-8
Nagano A, Hasegawa T, Ueki I, Ando K (2017) El Niño-Southern Oscillation-time scale covariation of sea surface salinity and freshwater flux in the western tropical and northern subtropical Pacific. Geophys Res Lett 44:6895–6903. https://doi.org/10.1002/2017GL073573
Nagano A, Ueki I, Hasegawa T, Ando K (2018) Ocean-atmosphere observations in Philippine Sea by moored buoy. In: OCEANS - MTS/IEEE Kobe Techno-Ocean (OTO), Kobe, Japan, pp 1–6. https://doi.org/10.1109/OCEANSKOBE.2018.8558886
Needler GT (1985) The absolute velocity as a function of conserved measurable quantities. Prog Oceanogr 14:421–429
Nitani H (1972) Beginning of the Kuroshio. In: Stommel H, Yoshida K (eds) Kuroshio-its physical aspects. University of Tokyo Press, Tokyo, pp 129–163
Olbers DJ, Wenzel M, Willebrand J (1985) The inference of North Atlantic circulation patterns from climatological hydrographic data. Rev Geophys 23(4):313–356
Pedlosky J (1987a) Geophysical fluid dynamics, 2nd edn. Springer, New York. https://doi.org/10.1007/978-1-4612-4650-3
Pedlosky J (1987b) Thermocline theories. In: Abarbanal HDI, Young WR (eds) General circulation of the ocean. Springer, Berlin, pp 55–88
Pujol M-I, Mertz F (2020) Product user manual for sea level SLA products. CMEMS, CMEMS
Qu T (2003) Mixed layer heat balance in the western North Pacific. J Geophys Res. https://doi.org/10.1029/2002JC001536
Qu T, Lukas R (2003) The bifurcation of the North Equatorial Current in the Pacific. J Phys Oceanogr 33:5–18
Qu T, Mitsudera H, Yamagata T (1998) On the western boundary currents in the Philippine Sea. J Geophys Res 103(C4):7537–7548
Ralph EA, Niiler PP (1999) Wind-driven currents in the tropical Pacific. J Phys Oceanogr 29(9):2121–2129
Reid JL (1997) On the total geostrophic circulation of the Pacific Ocean: flow patterns, tracers, and transports. Prog Oceanogr 39:263–352
Reynolds RW, Rayner NA, Smith TM, Stokes DC, Wang W (2002) An improved in situ and satellite SST analysis for climate. J Clim 15:1609–1625
Richards KJ, Natarov A, Firing E, Kashino Y, Soares SM, Ishizu M, Carter GS, Lee JH, Chang KI (2015) Shear-generated turbulence in the equatorial Pacific produced by small vertical scale flow features. J Geophys Res 120:3777–3791. https://doi.org/10.1002/2014JC010673
Rintoul SR, Sokolov S, Church J (2002) A 6 year record of baroclinic transport variability of the Antarctic Circumpolar Current at 140°E derived from expendable bathythermograph and altimeter measurements. J Geophys Res. https://doi.org/10.1029/2001JC000787
Rio MH, Guinehut S, Larnicol G (2011) New CNES-CLS09 global mean dynamic topography computed from the combination of GRACE data, altimetry, and in situ measurements. J Geophys Res. https://doi.org/10.1029/2010JC006505
Sasaki YN, Schneider N, Maximenko N, Lebedev K (2010) Observational evidence for propagation of decadal spiciness anomalies in the North Pacific. Geophys Res Lett. https://doi.org/10.1029/2010GL042716
Sato K, Suga T, Hanawa K (2004) Barrier layer in the North Pacific subtropical gyre. Geophys Res Lett. https://doi.org/10.1029/2003GL018590
Schmitz WJ Jr (1995) On the interbasin-scale thermohaline circulation. Rev Geophys 33(2):151–173. https://doi.org/10.1029/95RG00879
Schneider N, Miller AJ, Alexander MA, Deser C (1999) Subduction of decadal North Pacific temperature anomalies: observations and dynamics. J Phys Oceanogr 29:1056–1070
Stommel H, Schott F (1977) The beta spiral and the determination of the absolute velocity field from hydrographic station data. Deep-Sea Res 24:325–329
Sun C, Watts DR (2001) A circumpolar gravest empirical mode for the Southern Ocean hydrography. J Geophys Res 106(C2):2833–2855
Swart S, Speich S, Ansorge IJ, Lutjeharms JRE (2010) An altimetry-based gravest empirical mode south of Africa: 1. Development and validation. J Geophys Res. https://doi.org/10.1029/2009JC005299
Talley LD, Pickard GL, Emery WJ, Swift JH (2011) Descriptive physical oceanography: an introduction, 6th edn. Academic Press, Boston. https://doi.org/10.1016/C2009-0-24322-4
Tanaka Y, Hibiya T (2019) Generation mechanism of tropical instability waves in the equatorial Pacific Ocean. J Phys Oceanogr 49(11):2901–2915. https://doi.org/10.1175/JPO-D-19-0094.1
Thomson RE, Emery WJ (2014) Data analysis methods in physical oceanography, 3rd edn. Elsevier, Amsterdam. https://doi.org/10.1016/C2010-0-66362-0
Tourre YM, Rajagopalan B, Kushnir Y, Barlow M, White WB (2001) Patterns of coherent decadal and interdecadal climate signals in the Pacific Basin during the 20th century. Geophys Res Lett 28(10):2069–2072. https://doi.org/10.1029/2000GL012780
Tozuka T, Kagimoto T, Masumoto Y, Yamagata T (2002) Simulated multiscale variations in the western tropical Pacific: the Mindanao Dome revisited. J Phys Oceanogr 32:1338–1359
Trenberth KE (1997) The definition of El Niño. Bull Am Meteor Soc 78:2771–2777
Ward J (1963) Hierarchical grouping to optimize an objective function. J Am Stat Assoc 58:236–244. https://doi.org/10.2307/2282967
Whalen CB, Talley LD, MacKinnon JA (2012) Spatial and temporal variability of global ocean mixing inferred from Argo profiles. Geophys Res Lett. https://doi.org/10.1029/2012GL053196
White WB, Tourre YN, Barlow M, Dettinger M (2003) A delayed action oscillator shared by biennial, interannual, and decadal signals in the Pacific Basin. J Geophys Res. https://doi.org/10.1029/2002JC001490
Yamazaki A, Watanabe T, Tsunogai U, Iwase F, Yamano H (2016) A 150-year variation of the Kuroshio transport inferred from coral nitrogen isotope signature. Paleoceanography 31:838–846. https://doi.org/10.1002/2015PA002880

Publisher's Note